Arabian Journal of Chemistry (2023) **16**, 105160

King Saud University

Arabian Journal of Chemistry

www.ksu.edu.sa
www.sciencedirect.com

ORIGINAL ARTICLE

Sc^{3+}:Ce^{4+}:Y^{3+} doped zirconia nanopowders (ScCeYSZ): Synthesis, thermal phase stability and hot corrosion behavior of spark plasma sintered body

Mina Aflaki [a], Fatemeh Davar [a,*], Mohammad Reza Loghman Estarki [b], Ruixue Wang [c], Lei Guo [d]

[a] *Department of Chemistry, Isfahan University of Technology, Isfahan, Iran*
[b] *Department of Materials Eengineering, Malek Ashtar University of Technology, Isfahan, Iran*
[c] *Beijing University of Chemical Technology, College of Mechanical and Electrical Engineering, Beijing, China*
[d] *School of Materials Science and Engineering, Tianjin University, Tianjin 300072, China*

Received 30 May 2023; accepted 8 July 2023
Available online 17 July 2023

KEYWORDS

Stabilizer;
Nanoparticles;
Sintering;
Ceramics;
Phase stability;
Hot corrosion test

Abstract This study aims to investigate the high-temperature phase stability and hot corrosion behavior of zirconia with triple doping of Sc^{3+}, Ce^{4+} and Y^{3+} ions. FESEM result shows that the mean particle size of ScCeYSZ nanoparticles was 80–90 nm. Next, optimal samples regarding the highest high-temperature phase stability (1.9%Sc8.3%Ce1.8%YSZ, 1.1%Sc9.0%Ce1.8%YSZ and 0.5%Sc9.6%Ce1.8%YSZ) were consolidated at 1550 °C for 15 min via the spark plasma sintering (SPS) method. A hot corrosion test was done in the presence of 45%Na_2SO_4 + %55V_2O_5 salts on three samples at 900 °C for 2 h. Also, the results of hot corrosion were compared with ceramic resulting from the nanostructured YSZ bulk sample (nanoYSZ).

Based on the X-ray diffraction results, the formation of the non-transformable tetragonal phase is confirmed in the synthesized nanopowders. Also, the phase and microstructural results after hot corrosion of sintered samples show the formation of a monoclinic phase and destructive YVO_4 crystals and quasi-cubic CeO_2 crystals on the surface of sintered samples. The results indicated that the sample containing 1.8% scandia, 8.3% ceria, and 1.9% yttria had the highest phase stability and

---

* Corresponding author.
E-mail address: davar@cc.iut.ac.ir (F. Davar).

Peer review under responsibility of King Saud University.

Production and hosting by Elsevier

https://doi.org/10.1016/j.arabjc.2023.105160

hot corrosion resistance (low monoclinic percentage and low leaching of stabilizer elements of Sc^{3+}:Ce^{4+}:Y^{3+} from zirconia lattice and low depth of molten salt).

1. Introduction

Zirconia stabilized with yttria (YSZ) is used in various applications such as thermal insulation coatings, refractories in jet engines, and dental veneers due to its high melting temperature, low thermal conductivity, good chemical stability, and biocompatibility (Yuan et al., 2018). The use of polluted fuels, including V and S elements, cause hot corrosion of common 7% yttria-stabilized zirconia ceramics (7YSZ). Vanadium oxide (V_2O_5), sodium sulfate (Na_2SO_4) and sodium chloride (NaCl) are common impurities in the fuel used (Yuan et al., 2018; Zhang et al., 2019). During hot corrosion (at around 900 °C), yttria leached from the zirconia lattice, and the majority of the tetragonal phase of the zirconia transformed to a monoclinic phase and caused the failure of YSZ ceramics. Furthermore, zirconia has three structures (cubic, monoclinic and tetragonal). The tetragonal phase of YSZ (t-YSZ) transformed to a monoclinic phase at temperatures above ~ 1180 °C (Jones et al., 1996; Sadeghi et al., 2022; Guo et al., 2019; Khaki et al., 2022). Accheving non-transformable tetragonal "t′ phase" instead of transformable tetragonal "t phase" of zirconia are. important to have good mechanical and corrosion resistance properties for stabilized zirconia ceramics (Guo et al., 2019; Khaki et al., 2022; Habibi and Guo, 2015). The t′ -phase has higher phase stability than the t -phase due to the low leaching of the stabilizer agent from the zirconia lattice and has good teragonality ($c/a\sqrt{2}$) was close ~ 1).

Many attempts have been made to improve high-temperature phase stability and corrosion resistance by doping ceramic oxides such as CeO_2, Sc_2O_3, Al_2O_3, Yb_2O_3, TiO_2, Cd_2O_3, In_2O_3, MgO, etc. within zirconia lattice (Guo et al., 2019; Khaki et al., 2022; Habibi and Guo, 2015; Chen et al., 2019; Bokov et al., 2021; Hajizadeh-Oghaz et al., 2016; Liu et al., 2014; Dong et al., 2022; Radjehi et al., 2023; Jamali et al., 2014).

Many methods, such as hot pressing, hot isostatic pressing and SPS methods, are used to sinter metal oxide stabilized zirconia nanopowders. Today, the SPS method is widely used because of advantages such as short process time, smaller grain size, and preparation of samples with almost complete density at lower temperatures compared to conventional hot-press, microwave sintering and pressureless sinter (Ritasalo et al., 2013; Ahsanzadeh-Vadeqani and Razavi, 2016; Grabis et al., 2018; Kikuchi et al., 2018; Bat-Ulzii et al., 2023; Zhao et al., 2022; Jones et al., 1996; Huang et al., 2022). Extensive studies have been reported on the preparation of yttria-stabilized zirconia (Ahsanzadeh-Vadeqani and Razavi, 2016), ceria-stabilized zirconia (Grabis et al., 2018), and other zirconia-based ceramics (Kikuchi et al., 2018) via the SPS technique.

A study examined the effect of Sc_2O_3 content on the hot corrosion behavior of ScYSZ ceramics (x% mol Sc_2O_3-1.5% mol Y_2O_3 doped zirconia at 1000 °C (Chen et al., 2019). Experiments have shown that the tetragonal phase stability of the samples would grow with an elevation of the Sc_2O_3 content. It was reported that the reaction between the mixture of Na_2SO_4 + V_2O_5 molten salts and Y_2O_3 zirconia stabilizers produces rod-like YVO_4 crystals; indeed, it removes Y_2O_3 from the zirconia lattice, causing the conversion of zirconia phase from tetragonal to monoclinic (Jamali et al., 2014). Many studies have evaluated the hot corrosion behavior of Ytrria stabilized zirconia (YSZ, including one stabilizer agent), CYSZ (including two stabilizer agents: ZrO_2-25 wt% CeO_2-2.5 wt% Y_2O_3), and ScYSZ (including two stabilizer agent: ZrO_2-4.5 wt% Sc_2O_3-0.5 wt% Y_2O_3) (Bokov et al., 2021; Hajizadeh-Oghaz et al., 2016; Liu et al., 2014). However, so far, the hot corrosion behavior of Scandia-Ceria-Ytrria stabilized zirconia (ScCeYSZ, including three stabilizer agents) materials have not been examined.

Since the sol–gel method is a simple, low-cost method with good control of the stoichiometry of the final product, this method was considered for the synthesis of ScCeYSZ nanopowder. In this work, zirconia stabilized with various weight percentages of Sc^{3+}:Ce^{4+}:Y^{3+} (ScCeYSZ) was synthesized via the sol–gel method. Then, three samples with the highest phase stability at annealing temperatures (1600 °C) were selected and sintered through the SPS method. Ultimately, the hot corrosion behavior of the sintered ScCeYSZ was examined. Further, the hot corrosion results were compared with ceramic resulting from yttria-stabilized zirconia nanogranules (YSZ).

2. Experimental

2.1. Samples preparation

The $ZrOCl_2{\cdot}8H_2O$, $Y(NO_3)_3{\cdot}6H_2O$, $Ce(NO_3)_3{\cdot}6H_2O$ and $Sc(NO_3)_3{\cdot}6H_2O$ salts with a purity of 99.9% purchased from Merck (Germany) were chosen as the raw materials. Further,

Table 1 Weight percentages used in the synthesized ScCeYSZ nanoparticles.

Composition	wt% CeO_2	wt% Y_2O_3	wt% Sc_2O_3	Percentage of X_m (%)	Xt%
$(ScCeYSZ)_1$	8.3	1.9	1.8	0.14	99.82
$(ScCeYSZ)_2$	9.0	1.9	1.1	0.20	99.77
$(ScCeYSZ)_3$	9.6	1.9	0.5	0.29	99.69
$(ScCeYSZ)_4$	7.6	1.9	2.5	0.35	99.62
$(ScCeYSZ)_5$	6.9	1.9	3.2	0.40	99.57
$(ScCeYSZ)_6$	6.3	1.9	3.8	0.42	99.55
$(ScCeYSZ)_7$	5.5	1.9	4.6	0.51	99.46
$(ScCeYSZ)_8$	4.8	1.9	5.3	0.52	99.45
$(ScCeYSZ)_9$	4.0	1.9	6.1	0.57	99.40
$(ScCeYSZ)_{10}$	3.4	1.9	6.7	0.61	99.36
$(ScCeYSZ)_{11}$	2.8	1.9	7.3	1.04	98.93
$(ScCeYSZ)_{12}$	2.2	1.9	7.9	1.42	98.55
$(ScCeYSZ)_{13}$	1.4	1.9	8.7	2.21	97.76

yttria-stabilized zirconia nanogranules (nano8YSZ) were purchased from Sulzer Metko Co.

First, the $ZrOCl_2 \cdot 8H_2O$, $Y(NO_3)_3 \cdot 6H_2O$, $Ce(NO_3)_3 \cdot 6H_2O$ and $Sc(NO_3)_3 \cdot 6H_2O$ salts were dissolved in 100 mL of distilled water on a magnetic stirrer by maintaining a specific stoichiometric ratio (according to Table 1). Citric acid monohydrate was separately dissolved in distilled water with a Zr: CA mole ratio of 1:4. Next, citric acid solution was added to the zirconia and stabilizer salt solution and heated for 30 min at 50 °C. Thereafter, ethylene glycol with molar ratio (Zr:EG: CA = 1:4:4) was added to the solution and heated for 1 h at 80 °C. Subsequently, the temperature was elevated up to around 120 °C up to the desired gel would form. Next, to obtain the dry gel, the temperature was elevated up to 250 °C. After that, the dried gel was annealed at 800 °C, 1000 °C, and 1600 °C for 2 h. Also, high-temperature annealing (1600 °C/5h) was selected to explore the phase stability of zirconia and the monoclinic percentage of the samples.

According to Table 1, three samples $(ScCeYSZ)_1$, $(ScCeYSZ)_2$ and $(ScCeYSZ)_3$ with the highest phase stability at high temperature were selected as the best samples and the hot corrosion test were continued on these three samples.

2.2. Consolidation of $(ScCeYSZ)_{1\text{-}3}$ samples

Before sintering nanopowders, the samples ($(ScCeYSZ)_1$, $(ScCeYSZ)_2$ and $(ScCeYSZ)_3$ nanopowders calcined at a temperature of 1000 °C) were deagglomarated with the ball milling method. To ball mill, the powders obtained by the sol–gel method, a zirconia ball-to-powder ratio of 1 to 10 and a rotation speed of 300 rpm in zirconia chambers for 6 h were used. Then the ground samples were passed through a 300-mesh sieve.

The powder mixture obtained from the grinding stage was loaded into a graphite mold covered with graphite foil, and the spark plasma sintering process (SPS10Ton – 10,000 Amper, Iran) was carried out. The parameters of pressure, temperature and duration of sintering during the SPS process are 40 MPa, 1550 °C and 15 min, respectively. The temperature-increasing rate was 50 °C/min. After the spark plasma annealing process, disc-shaped samples with a diameter of 20 mm and a height of 10 mm were made. To remove the graphite layers from the surface of the samples, the samples were polished using sandpaper (Budi et al., 2022; Salahdin et al., 2022). The density of the samples was measured by Archimedes method and using distilled water as an immersion solvent.

2.3. Hot corrosion tests

A mixture of 45%Na_2SO_4 and 55% V_2O_5 powders was chosen as corrosive salts in this research (Jamali et al., 2014). The properties of the corrosive salts are reported in Table S1 (see supporting information) (Jamali et al., 2014). To evaluate the hot corrosion resistance of corrosive powders with a concen-

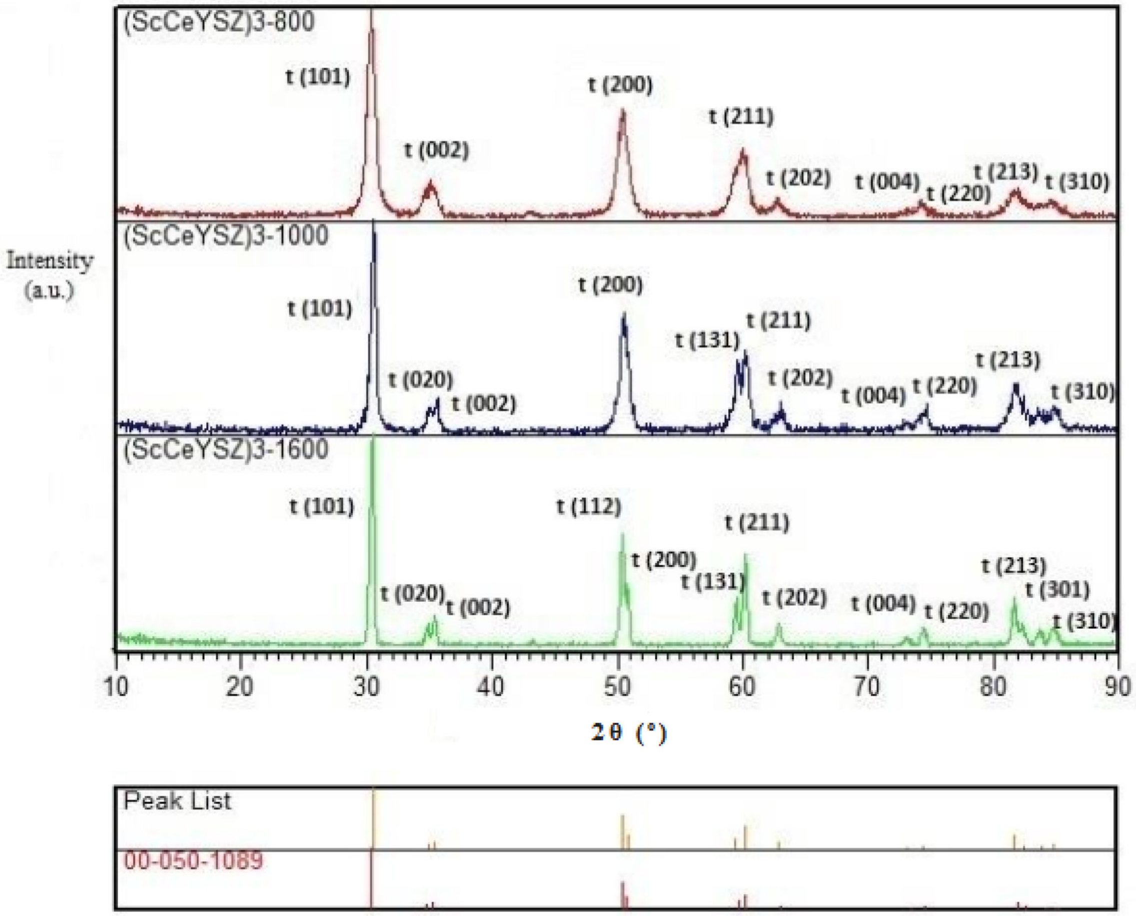

Fig. 1 XRD pattern of the $(ScCeYSZ)_3$ powders at annealing temperatures of 800, 1000, and 1600 °C/2h.

tration of 10 mg/cm^2 (Hajizadeh-Oghaz et al., 2016), at a distance of 1 cm from the edge, on the surface of the sample number of $(ScCeYSZ)_1$, $(ScCeYSZ)_2$ and $(ScCeYSZ)_3$ with a diameter of 20 mm and a height of 10 mm was done to spread a uniform level of corrosive powders on the disc surface. The corrosion test was performed at 900 °C for 2 h) (Hajizadeh-Oghaz et al., 2016; Jamali et al., 2014). Further, the hot corrosion output was compared with sintered yttria-stabilized zirconia (8YSZ, Sulzer Metko Co.). The percentage of holes was measured from a polished cross-section SEM image of ceramics by Image J software.

2.4. Characterization tests

The phase structure of the samples was analyzed through X-ray diffraction (Al-Zuhairy et al., 2022; Kadhum et al., 2022; Chupradit et al., 2022; Sivaraman et al., 2022; Obaid et al., 2022; Raya et al., 2022b) (XRD, Bruker D8 Advance) using Cu k_α (λ = 0.15406 nm, with a step size of 0.02° and time per step of 1 S).

The width of the peak at half the height of the maximum (FWHM) (Kadhim et al., 2022; Jasim, Hachem et al., 2022; Jasim, Hadi et al., 2022) was considered from the peak with the highest intensity located at 2θ of 30°.

The amount of phase stability is calculated from the volume fraction of the tetragonal phase (X_t, Equation (1) and the amount of phase transformation from the tetragonal to the monoclinic phase (X_m, Equation (2) (Rocha et al., 2022; Lughiw and Clarke, 2005; Jiang et al., 2018).

$$X_t = 0.88\frac{I_t(220)}{I_t(220) + I_t(004)} \tag{1}$$

$$X_m = \frac{I_m(1^{-}11) + I_m(111)}{I_m(1^{-}11) + I_m(111) + I_t(101)} \tag{2}$$

where I_m $(1^{-}11)$ represents the intensity of the diffraction peak at 2θ = 28°, I_m (111) shows the intensity of the diffraction peak at 2θ = 31° for the monoclinic phase, and I_t (101) denotes the intensity of the diffraction peak at 2θ = 30° for the tetragonal phase. I_t(004) and I_t (220) represents diffraction intensity at 2θ of 73° and 74° of the tetragonal phase. For further analysis of the phase structure in the samples, Raman spectroscopy (Plasmonic, Iran) was used with an excitation wavelength of 532 nm via argon ion laser (Yumashev et al., 2022).

The microstructural properties of the samples were examined through field emission scanning electron microscopy (FESEM) (FEI model, USA) (Seyyedi et al., 2021; Dmytro, 2020; Kadhum et al., 2021) equipped with Energy Dispersive X-ray Spectroscopy (EDS) (Chen et al., 2023; Zhang et al., 2023; Kartika et al., 2022).

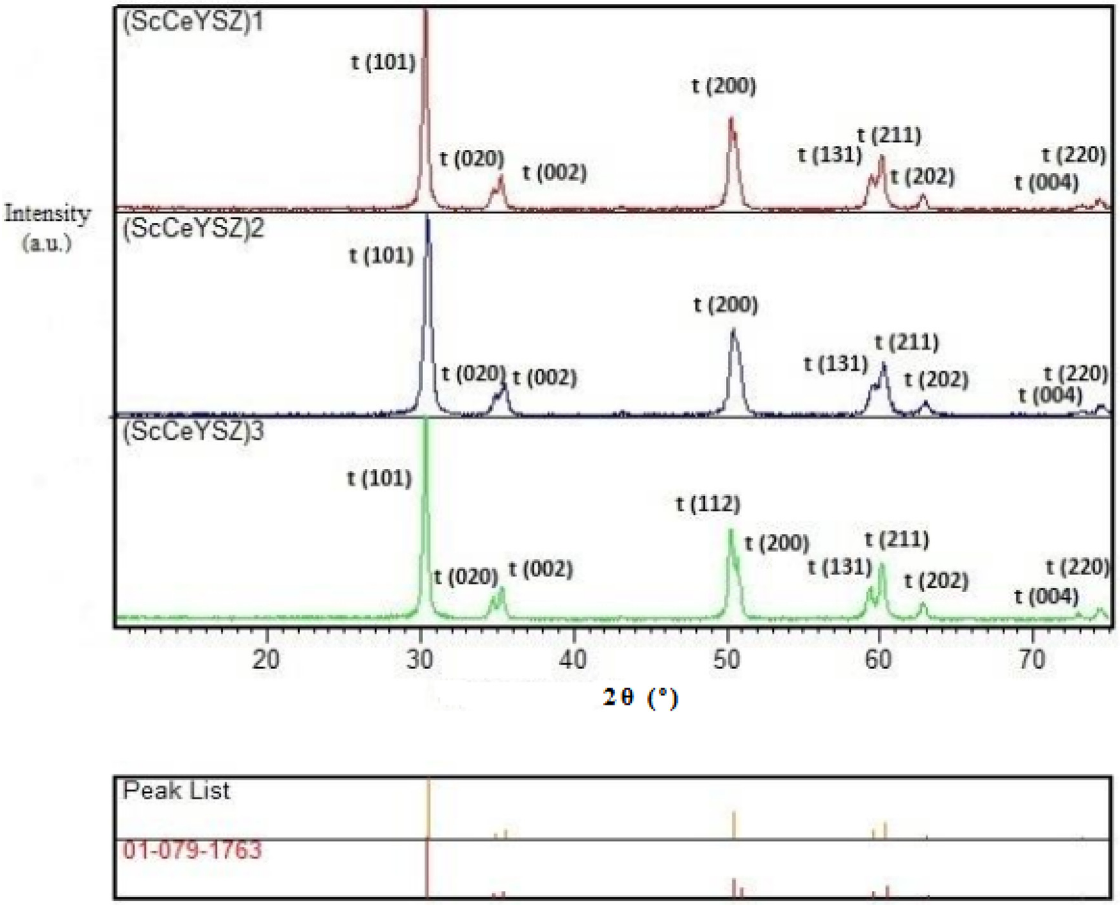

Fig. 2 XRD pattern of three powders $(ScCeYSZ)_{1-3}$ at an annealing temperature of 1000 °C for 2 h.

3. Results and discussion

3.1. XRD analysis of nanoparticles

The XRD pattern of $(ScCeYSZ)_3$ sample annealed at 800, 1000, and 1600 °C is shown in Fig. 1. The JCPDS card number and its standard peak list are specified under the XRD patterns. It is seen that no impurity, including Sc_2O_3, Y_2O_3, and CeO_2, was detected in the XRD pattern. This suggests that all stabilizers have been successfully doped within the zirconia lattice. The main diffractions of the tetragonal phase have occurred at $2\theta = 30°, 35°, 50°, 60°, 73°, 74°$, which are related to the reflection of (101), (002), (200), (211), (004), and (400) planes respectively. The XRD patterns of tetragonal and cubic zirconia phases are similar, and it is difficult to distinguish between tetragonal and cubic zirconia (Srinivasan et al., 1991). Typically, the bifurcation of the (002/004) diffractions at $2\theta = 50°, 60°, 73°$ is related to the tetragonal phase (t-phase) (Li et al., 2022; Zhao et al., 2020). The larger the distance between the two peaks at $2\theta = 73°, 74°$, which are related to (004) and (400) planes, the greater the tetragonality parameter will be, where the tetragonal phase will have greater stability (Yuan et al., 2018; Zhang et al., 2019; Jones et al., 1996; Sadeghi et al., 2022; Guo et al., 2019; Li et al., 2022; Zhao et al., 2020; Chen et al., 2022; Song et al., 2023; Jalil Abduladheem et al., 2021; Li et al., 2021; Viazzi et al., 2006). As seen in Fig. 1, with an elevation of annealing temperature from 800 °C to 1600 °C, the distance between the two peaks at 74° will increase, and the tetragonal phase in the sample with an annealing temperature of 1000 °C is higher than at 800 °C. Due to the higher tetragonal phase volume percent at 1000 °C, this temperature was selected for the calcination of other samples. In all (ScCeYSZ) samples annealed at 800 °C, full width at half of the maximum peaks (FWHM) was lower than at 1000 °C and 1600 °C. This suggests that the crystallite size of the sample annealed at 800 °C is smaller than that of the sample annealed at 1000 °C and 1600 °C (according to Table S2, see supporting information). Furthermore, with increasing annealing temperature from 800 °C to 1000 °C, the crystallintty of ScCeYSZ was improved due to higher intensity of diffraction patterns. The rectangle below the XRD patterns belongs to matched standard peak list. The tetragonality $(c/a\sqrt{2})$ for the non-transformable tetragonal phase (t$'$ phase) tends to be 1.01, while for the transformable tetragonal phase, it is larger than 1.01 (Viazzi et al., 2006). Tetragonality for the $(ScCeYSZ)_3$ sample with an annealing temperature of 800 °C has been 1.02, while for the $(ScCeYSZ)_3$ sample at annealing temperatures of 1000 °C and 1600 °C, it has been 1.01.

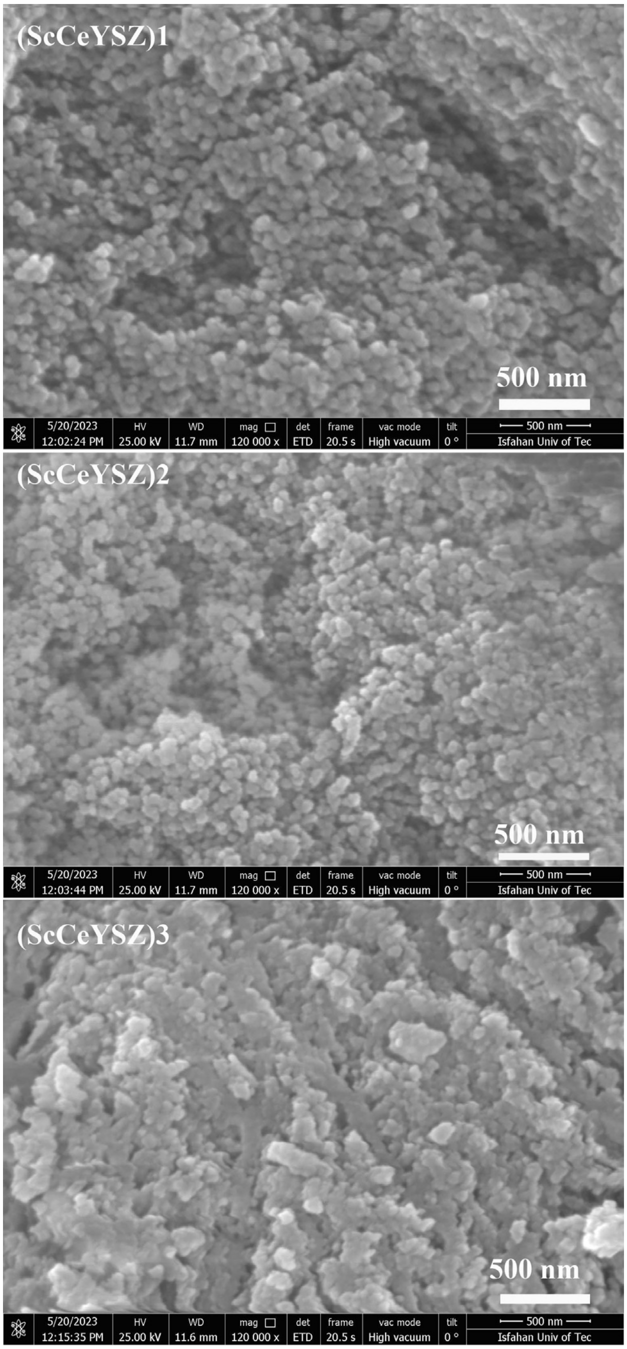

Fig. 3 FESEM images of $(ScCeYSZ)_{1\text{-}3}$ nanopowders at an annealing temperature of 1000 °C for 2 h.

Fig. 2 displays the XRD pattern of $(ScCeYSZ)_{1\text{-}3}$ samples with an annealing temperature of 1000 °C. As seen, the main phase in all samples is tetragonal, with no monoclinic phase identified in the samples. The value of the parameter $(c/a\sqrt{2})$ in $(ScCeYSZ)_1$, $(ScCeYSZ)_2$, and $(ScCeYSZ)_3$ have been 1.0039, 1.0083, and 1.0063 respectively. This confirms the formation of the phase in all three samples. The XRD pattern of the nanogranule (Fig. S1, see supporting information) also confirms its tetragonality.

Fig. 3 depicts the FESEM images of ScCeYSZ nanoparticles obtained at 1000 °C after 2 h. In all nanopowders, quasi-spherical particles have been synthesized. The particle size synthesized in $(ScCeYSZ)_{1\text{-}3}$ sample is between 80 and 90 nm. According to spot-size EDS analysis (Fig. 4), cerium, yttrium, zirconium, and oxygen exist in the EDS analysis of the three samples.

The stability of the tetragonal phase at 1600 °C for $(ScCeYSZ)_{1\text{-}3}$ samples is shown in Fig. 5. It is seen that even at 1600 °C, a phase transition has not occurred.

As observed in Fig. S2 (see supporting information), $(ScCeYSZ)_4$ and $(ScCeYSZ)_5$ samples contain a tetragonal phase. The larger the distance between two peaks at $2\theta = 7$

3°,74°, which are related to the reflection of (400) and (004) planes, the greater the tetragonality parameter will be, and the tetragonal phase will have greater stability. Indeed, the distance of the two peaks at 74° among the $(ScCeYSZ)_{1\text{-}5}$ samples has been the maximum inter-peak distance (see Fig. 5 and Fig. S2-S4, see supporting information). This suggests that the tetragonal phase in $(ScCeYSZ)_{1\text{-}5}$ samples has been more stable than other samples. Further, the $(ScCeYSZ)_{6\text{-}13}$ samples (Figs. S5 and S6) have a cubic phase.

Fig. 6 reveals the XRD pattern of samples synthesized at 1550 °C under a pressure of 40 MPa for 15 min. As seen, in all samples $(ScCeYSZ)_{1\text{-}3}$ and nanoYSZ, the major phase is tetragonal, and there is a little monoclinic phase in $(ScCeYSZ)_{1\text{-}3}$ samples. After SPS treatment, some Ce^{4+} leached from the ScCeYSZ sample, especially $(ScCeYSZ)_2$ and thus caused the transformation of the t-to-m phase (monoclinic phase) of zirconia. The peaks at $2\theta = 28°$ and 31° are related to the monoclinic phase. In the samples sintered at

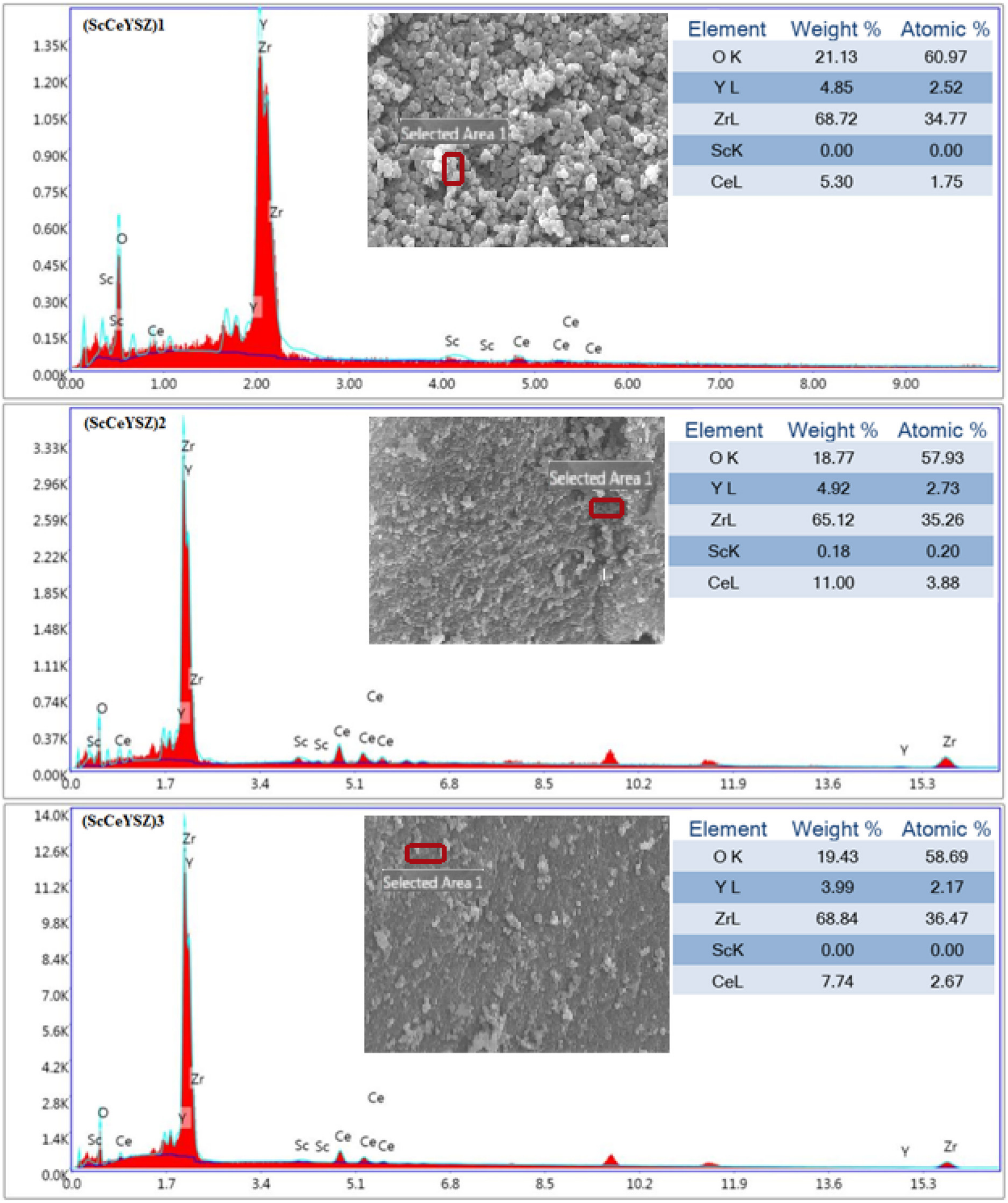

Element	Weight %	Atomic %
O K	21.13	60.97
Y L	4.85	2.52
ZrL	68.72	34.77
ScK	0.00	0.00
CeL	5.30	1.75

Element	Weight %	Atomic %
O K	18.77	57.93
Y L	4.92	2.73
ZrL	65.12	35.26
ScK	0.18	0.20
CeL	11.00	3.88

Element	Weight %	Atomic %
O K	19.43	58.69
Y L	3.99	2.17
ZrL	68.84	36.47
ScK	0.00	0.00
CeL	7.74	2.67

Fig. 4 EDS analysis of $(ScCeYSZ)_{1\text{-}3}$ powders at an annealing temperature of 1000 °C for 2 h.

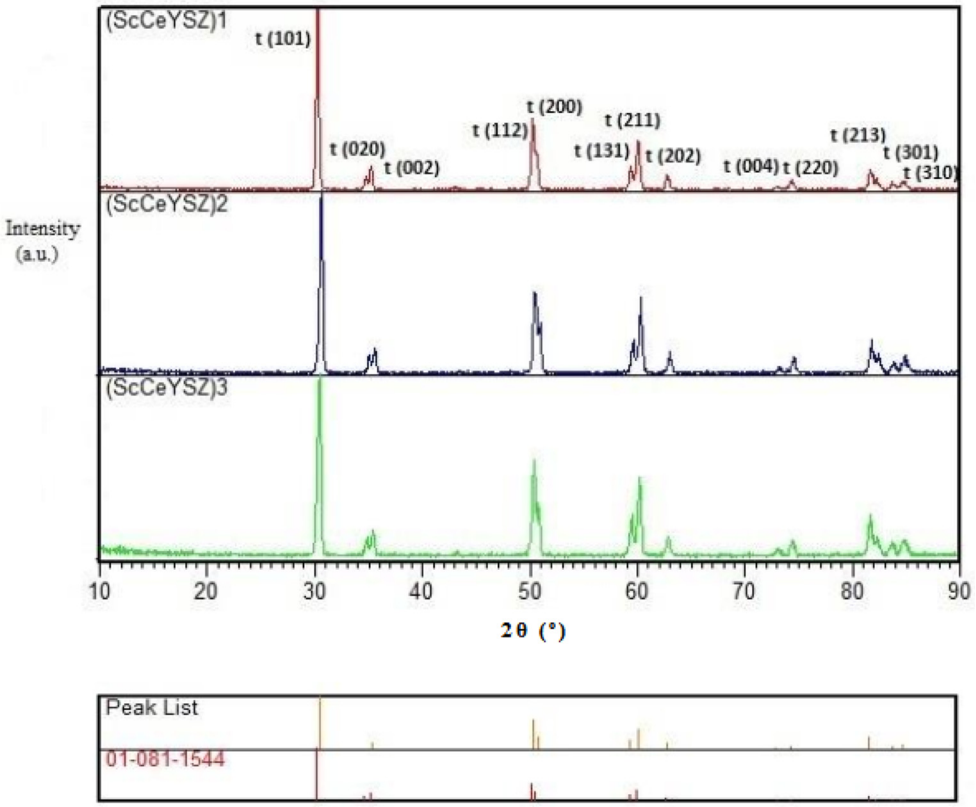

Fig. 5 XRD sample of $(ScCeYSZ)_{1\text{-}3}$ powders at an annealing temperature of 1600 °C for 2 h.

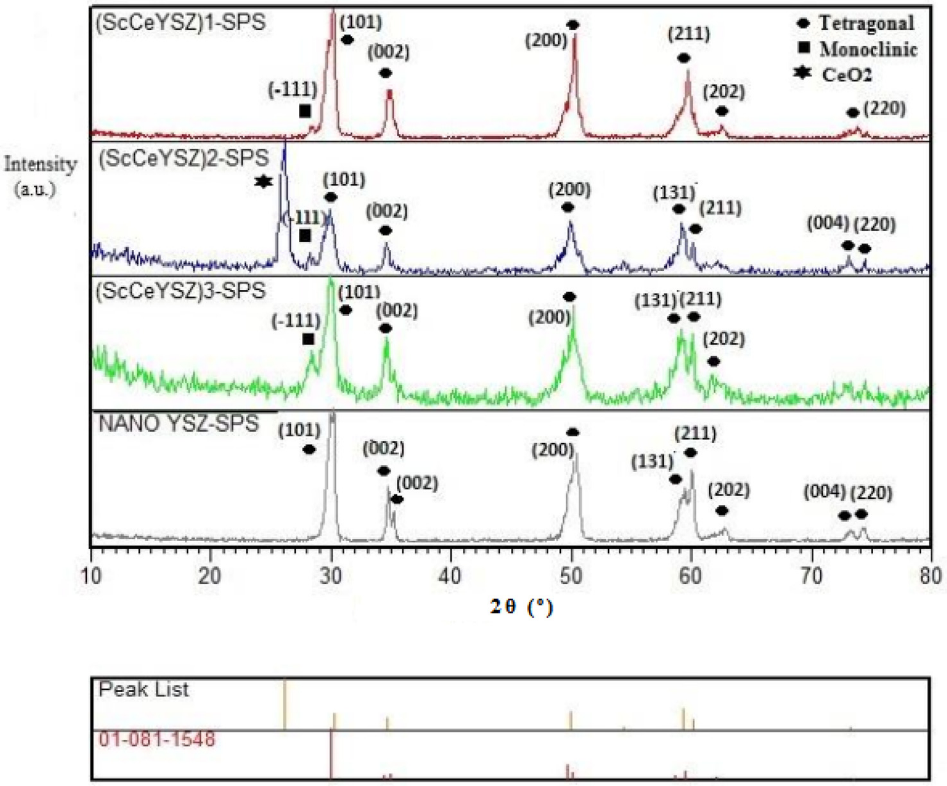

Fig. 6 XRD pattern of $(ScCeYSZ)_{1\text{-}3}$ and nano8YSZ nanopowders sintered at 1550 °C under the pressure of 40 MPa for 15 min.

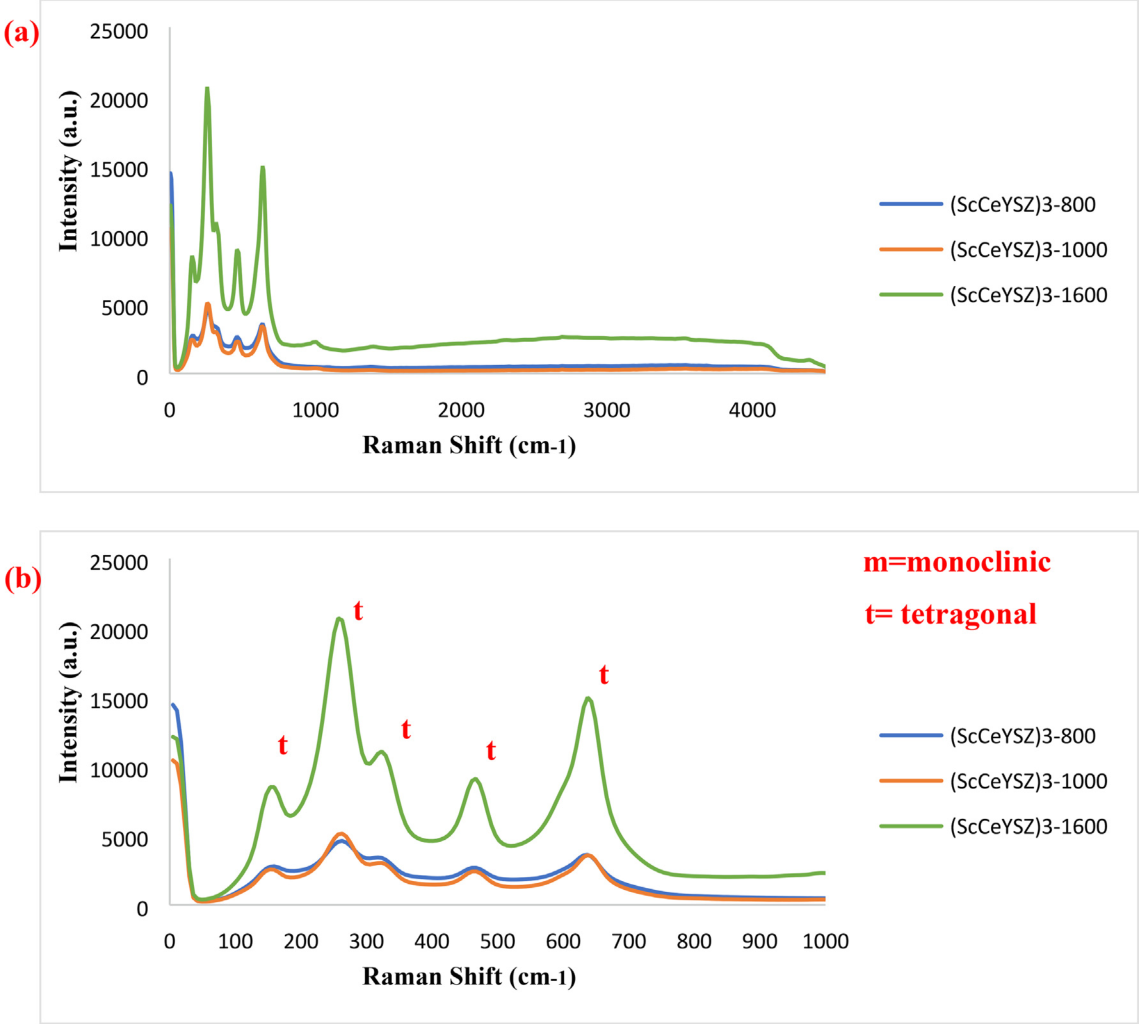

Fig. 7 Raman spectra of $(ScCeYSZ)_3$ powders at an annealing temperature of 800 °C, 1000 °C, and 1600 °C for 2 h (a) at a wavenumber of 100–4500 cm^{-1} (b) 100–1000 cm^{-1}.

Table 2 Raman shift of different modifications in zirconia Raman analysis (Lughiw and Clarke, 2005; Jiang et al., 2018; Bakhshkandi and Ghoranneviss, 2019).

Zirconia Phase	Raman Shift (cm^{-1})	Mode
Amorphous	550–600 (broad)	–
Monoclinic	98–102, 180–189, 220, 178, 189, 225, 300, 335, 380, 475. 535, 555, 615, 635	$9A_1g$ + 9Bg
Tetragonal	131–155, 240–266, 290–330, 410–475, 550–615, 616–645	$1A_1g$ + $2B_1g$ + 3Eg
Cubic	250–280, 464–490, 530–640	T_2g

1550 °C, some of the tetragonal phase has been converted to a monoclinic phase. The volumetric percentage of the tetragonal phase calculated through Eq. (1) in $(ScCeYSZ)_1$, $(ScCeYSZ)_2$, $(ScCeYSZ)_3$, and nanoYSZ has been 93.09, 86.34, 73.58, and 92%, respectively. With increasing the amount of scandia in the $(ScCeYSZ)_{1\text{-}5}$ sample, the percentage of the monoclinic phase was reduced, and the dominant phase in the sample is tetragonal. On the other hand, upon enhancing ceria in the zirconia lattice stabilized with yttria-ceria-scandia, the percentage of the monoclinic phase was increased. This issue is probably because the effective radius of the Ce^{4+} ion in ScCeYSZ ceramic is larger than Zr^{4+} and the zirconia lattice expands towards the monoclinic structure (this result was confirmed by Raman spectroscopy). Moreover, the effective radius of Sc^{3+} ion in ScCeYSZ ceramic is smaller than Zr^{4+}, and the zirconia network change to the cubic phase for $(ScCeYSZ)_{6\text{-}13}$ (confirmed by Raman spectroscopy).

3.2. Raman spectroscopy

Raman spectroscopy is employed for identifying and confirming different polymorphs of zirconia structure. Since the peaks of the cubic phase coincide with the tetragonal zirconia in XRD patterns, Raman analysis was taken (Nakamoto, 2006). Fig. 7 indicates the Raman spectra of $(ScCeYSZ)_3$ samples annealed at 800 °C, 1000 °C, and 1600 °C. Table 2 shows

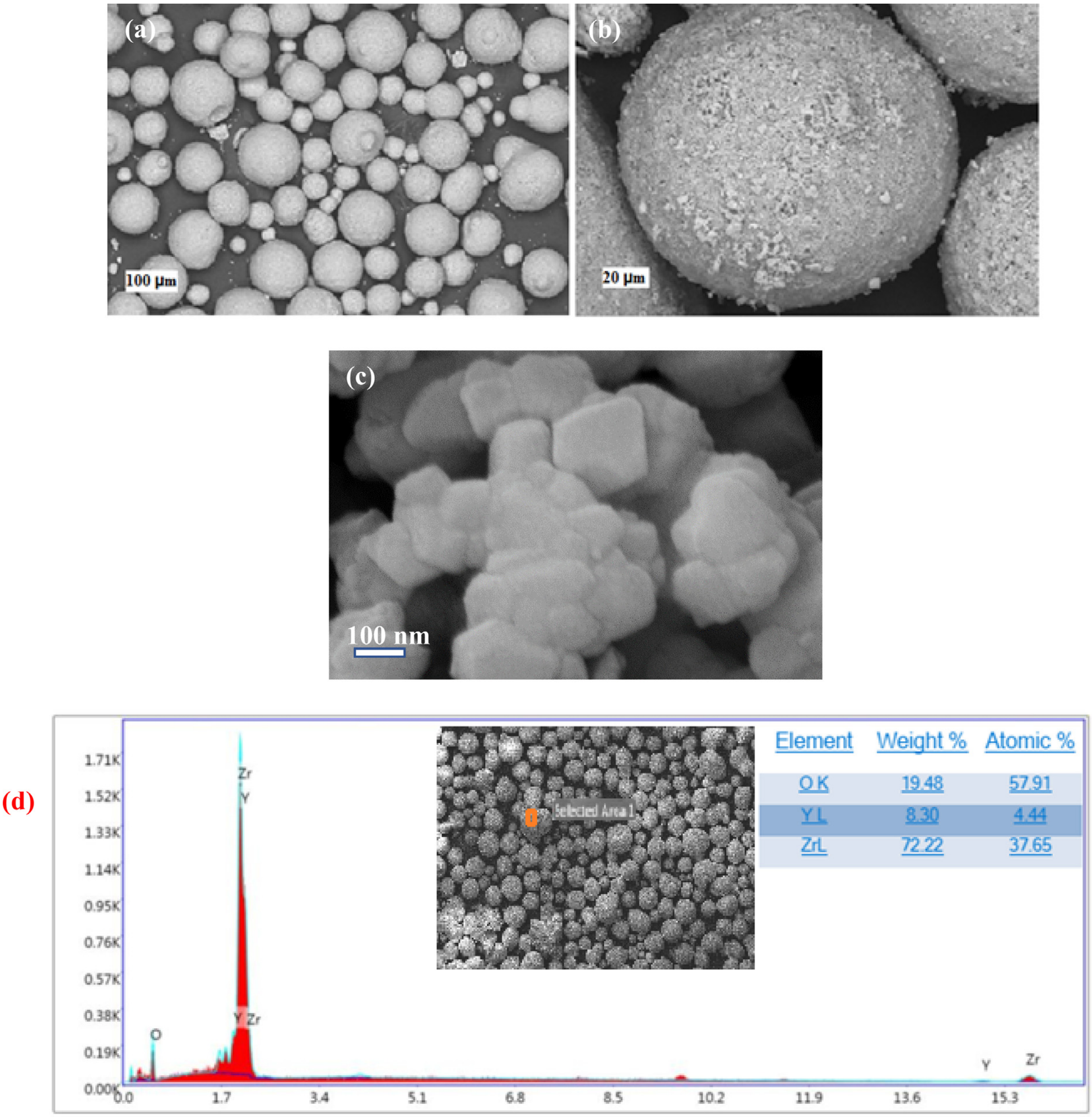

Element	Weight %	Atomic %
O K	19.48	57.91
Y L	8.30	4.44
Zr L	72.22	37.65

Fig. 8 (a-c) FESEM images (d) EDS analysis of the commercial 8YSZ nanogranule powders with different magnifications.

various Raman scattering peaks of zirconia phases (Dayal et al., 1992; Rashad and Baioumy, 2008; Kanade et al., 2008; Davar and Loghman-Estarki, 2014; Jasim et al., 2022b; Zhao et al., 2022; Raya et al., 2022a). The peaks at 153, 263, 467, and 637 cm^{-1} are related to the $2B_1g$, A_1g, and 3Eg vibrational modes of the zirconia tetragonal phase, respectively. The results of Raman analysis are in line with XRD findings. The cubic structure of zirconia has some bands at a larger wavelength at 4400 cm^{-1} (anti-stock peak), attributed to the fluorescence peaks, while for the tetragonal phase, no peak is seen in this region (Davar and Loghman-Estarki, 2014). In $(ScCeYSZ)_4$ and $(ScCeYSZ)_5$ samples, no peak is observed at 4400 cm^{-1} (Fig. S5, see supporting information), confirming the formation of the tetragonal phase. On the other hand, the $(ScCeYSZ)_{6\text{-}13}$ samples (Fig. S6, see supporting information) have a cubic phase. According to the results of XRD and Raman spectrum of samples calcined at 1000 °C, it was found that the synthesized samples $(ScCeYSZ)_{1\text{-}5}$ have a tetragonal phase. To check the stability of the tetragonal phase at high temperature, these samples were calcined at 1600 °C, and according to the XRD results, the synthesized samples $(ScCeYSZ)_{1\text{-}5}$ have a tetragonal phase. Among samples $(ScCeYSZ)_{1\text{-}5}$, three samples $(ScCeYSZ)_1$, $(ScCeYSZ)_2$ and $(ScCeYSZ)_3$ which had the lowest percentage of monoclinic phase and the highest stability of tetragonal phase at high temperature (1600 °C) were selected as optimal samples. Furthermore, as-synthesized $(ScCeYSZ)_{6\text{-}13}$ have a cubic phase.

3.3. Morphology of sintered sample before hot corrosion

FESEM images of the purchased powders can be seen in Fig. 8. The nanoYSZ powder contains spherical granules with an average size of 50–60 μm (Fig. 8a, b). The image with a lar-

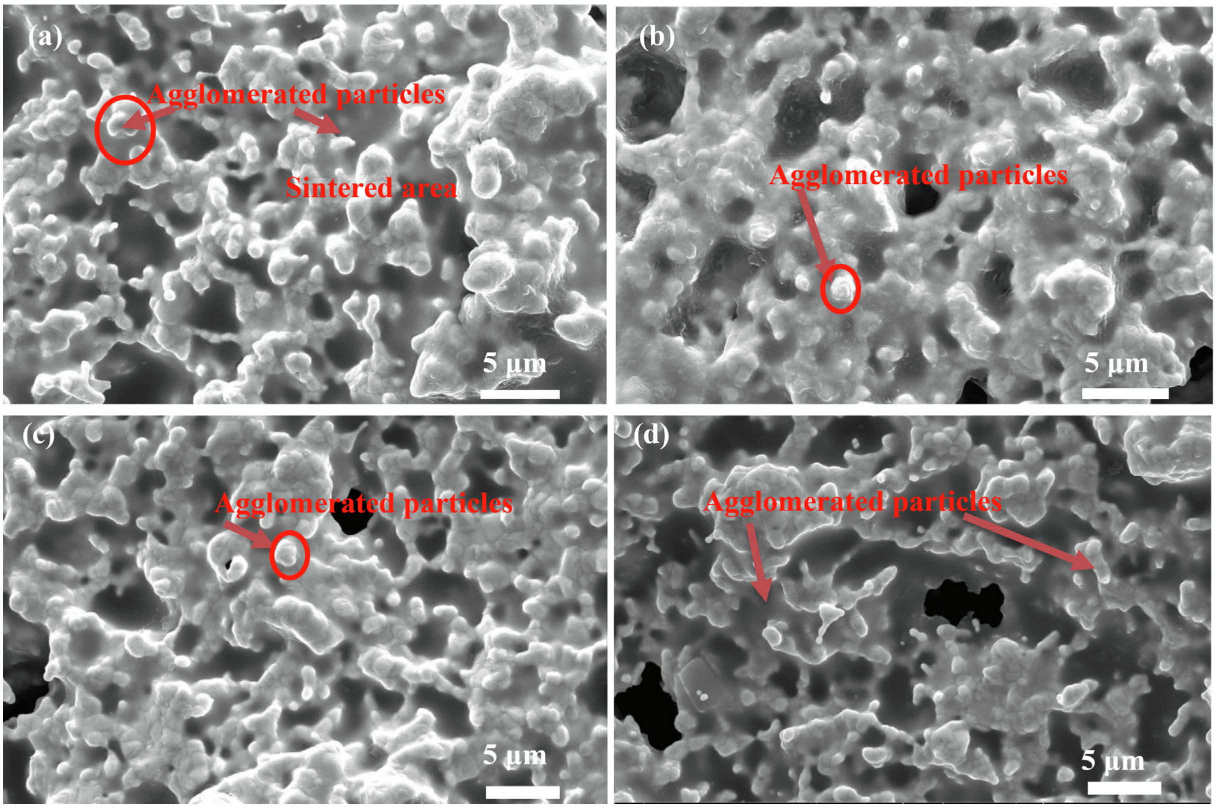

Fig. 9 SEM image from the surface of sintered (a) $(ScCeYSZ)_1$, (b) $(ScCeYSZ)_2$, (c) $(ScCeYSZ)_3$, and (d) nano8YSZ ceramics samples after annealing etching at 1400 °C for 4h.

ger magnification of this sphere shows that any sphere is an aggregation of 60–80 nm nanoparticles (Fig. 8c). Also, based on EDS analysis in Fig. 8d, zirconium, yttrium, and oxygen elements exist in the YSZ nanogranule.

Fig. 9 reveals the SEM image of the surface of sintered samples. According to Fig. 9, the particle size of all nanopowders was increased from 80 to 90 nm to micrometer size. The image also shows aggregated particles across the surface of the sample. As seen, the sintered areas are discrete and are interlinked to each other with closed pores.

According to fractured cross-sectional FESEM images of sintered $(ScCeYSZ)_{1\text{-}3}$ sample, the grain size of $(ScCeYSZ)_{1\text{-}3}$ was between 200 and 300 and the grain size of nanoYSZ ceramics was 400–500 nm (Fig. S7, see supporting information file).

Fig. 10 exhibits the EDS analysis of the sintered samples before the hot corrosion test. According to this test, the stabilizer percentages are different from the experimentally added percentages.

The density for the nanoYSZ, $(ScCeYSZ)_1$, $(ScCeYSZ)_2$, and $(ScCeYSZ)_3$ samples were obtained at 98, 98.9, 100, and 100%, respectively.

3.4. Hot corrosion behavior

Fig. 11 depicts the XRD pattern of the samples after hot corrosion in Na_2SO_4 + V_2O_5 molten salts at 900 °C for 2 h. The volume fraction of monoclinic phase in samples $(ScCeYSZ)_1$, $(ScCeYSZ)_2$, $(ScCeYSZ)_3$ and nano YSZ is equal to 20.24%, 23.68%, 79.56% and 89.0%, respectively. The monoclinic phase content in the nanoYSZ sample has more than the other one, indicating that most Y^{3+} leached from the zirconia lattice after the hot corrosion test.

Based on the XRD results of samples pre-corrosion, the $(ScCeYSZ)_3$ sample has had a greater monoclinic phase compared to other samples, and thus the greatest extent of corrosion is seen in this sample. The volumetric fraction of the monoclinic phase functions as a criterion for the instability of bulk samples along the hot corrosion test (Table 3).

According to Table 3, the ScCeYSZ show the lowest volumetric percentages of the monoclinic phase before and after the hot corrosion test.

In the nanoYSZ sample, after the hot corrosion, it is evident that the tetragonal peak at $2\theta = 30°$ has diminished, and the main product of YVO_4 has been produced at $2\theta = 26°$. Among the samples, $(ScCeYSZ)_1$ sample has shown the minimum extent of the corrosion, while $(ScCeYSZ)_3$ has indicated the greatest extent of corrosion. Based on the results, it can be confirmed that in the presence of Na_2SO_4 + V_2O_5 molten salts, the $(ScCeYSZ)_1$ sample shows better phase stability compared to other samples and is more resistant to corrosion. Hot corrosion occurs when Na_2SO_4 + V_2O_5 molten salts react with the stabilizers in zirconia and lead to the outflow of stabilizers from within the zirconia structure. This causes a reduction of the tetragonal phase and its conversion to the monoclinic phase, eventually resulting in surface corrosion. The amount of YVO_4 corrosion product has increased in the nanoYSZ sample. The reaction of vanadium oxide and sodium

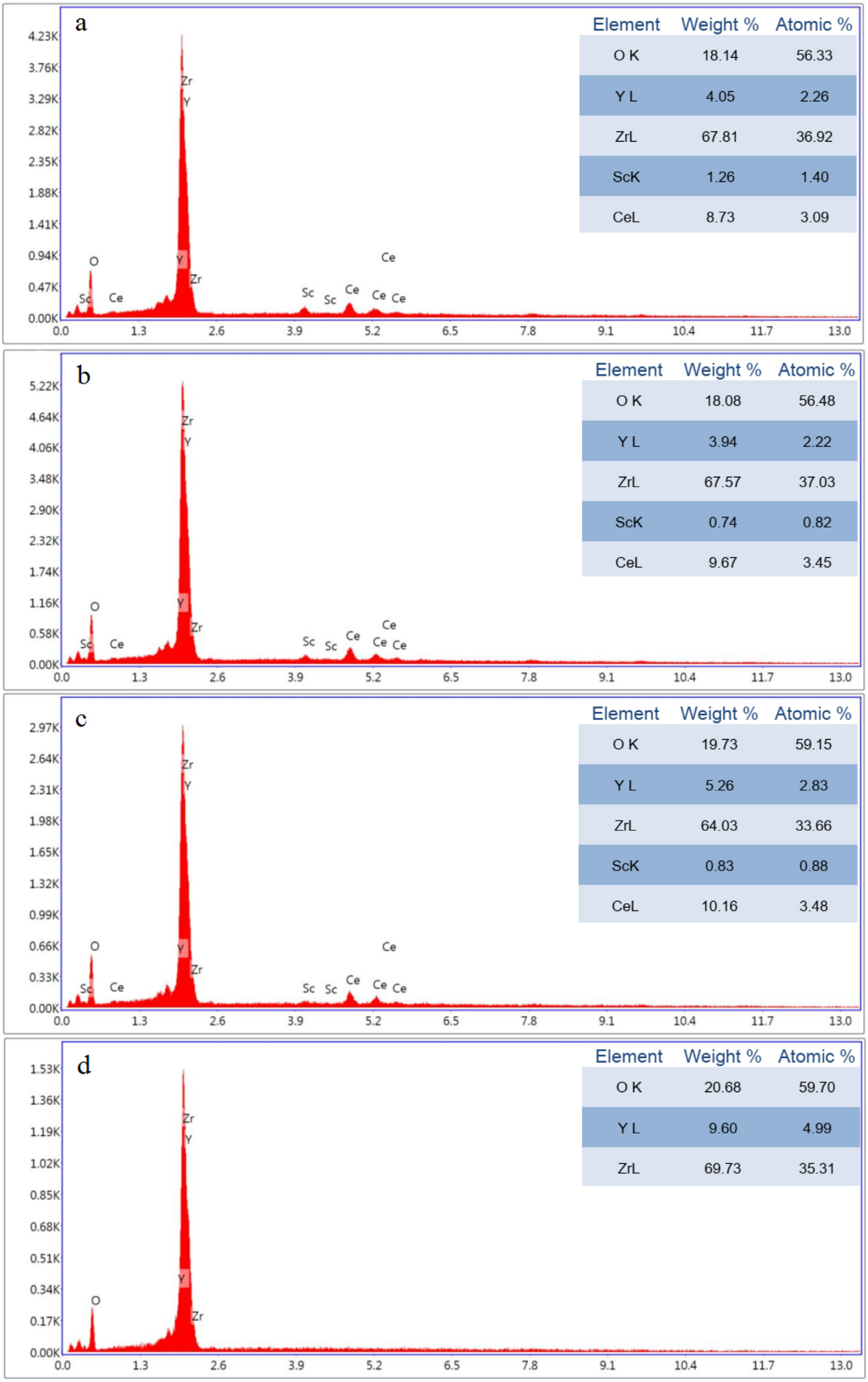

Element	Weight %	Atomic %
O K	18.14	56.33
Y L	4.05	2.26
ZrL	67.81	36.92
ScK	1.26	1.40
CeL	8.73	3.09

Element	Weight %	Atomic %
O K	18.08	56.48
Y L	3.94	2.22
ZrL	67.57	37.03
ScK	0.74	0.82
CeL	9.67	3.45

Element	Weight %	Atomic %
O K	19.73	59.15
Y L	5.26	2.83
ZrL	64.03	33.66
ScK	0.83	0.88
CeL	10.16	3.48

Element	Weight %	Atomic %
O K	20.68	59.70
Y L	9.60	4.99
ZrL	69.73	35.31

Fig. 10 EDS of spark plasma sintered bodies of (a) (ScCeYSZ)$_1$, (b) (ScCeYSZ)$_2$, (c) (ScCeYSZ)$_3$, and (d) nano8YSZ samples.

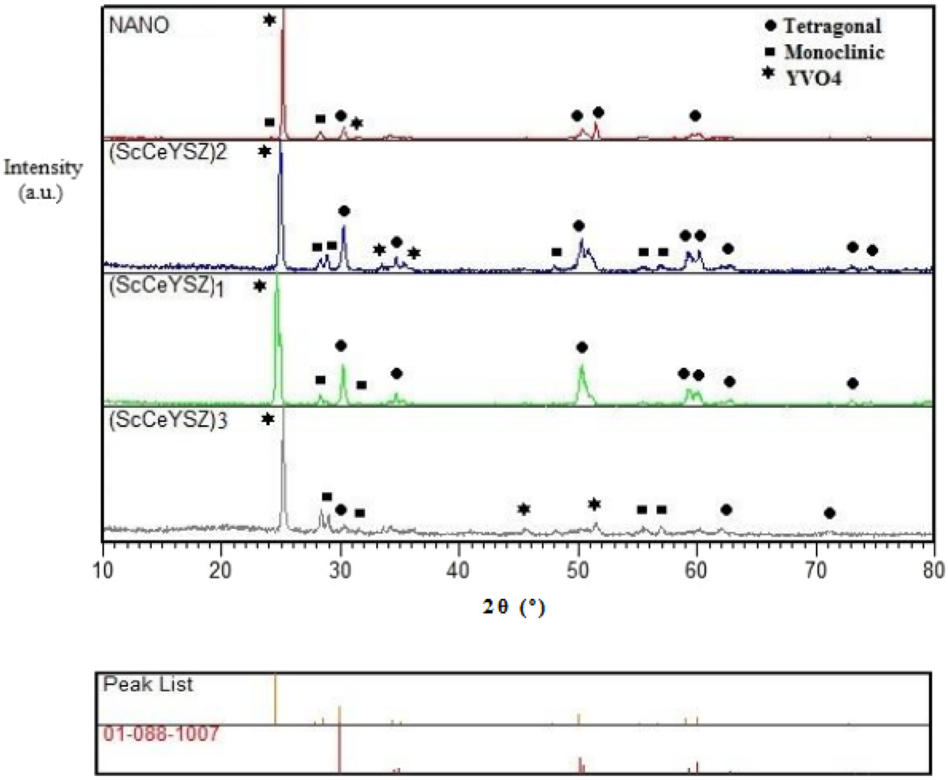

Fig. 11 XRD pattern of the three samples $(ScCeYSZ)_{1\text{-}3}$ and nano 8YSZ bulk samples after hot corrosion test.

Table 3 The calculated volume percentage of the monoclinic phase of the samples before and after the corrosion test.

Composition	Percentage of X_m (%) before corrosion	Percentage of X_m (%) after corrosion
$(ScCeYSZ)_1$	6.91	20.24
$(ScCeYSZ)_2$	13.66	23.68
$(ScCeYSZ)_3$	26.42	79.56
Nano 8YSZ	8	89

sulfate leads to the formation of sodium vanadate at 900 °C. Since this salt has a low melting point of 610 °C, at 900 °C along the hot corrosion test, $NaVO_3$ ions have excellent mobility and diffusivity. As such, they can diffuse into the ceramics through the microcracks and pores present in the surface, and react with Y_2O_3 present in the zirconia structure, thus producing YVO_4 (Chen et al., 2019). This reduction of stabilizers from inside the zirconia structure results in a reduction of the tetragonal phase and accelerates the course of corrosion. It is seen that although the third sample has had the largest theoretical density (100%), its hot corrosion resistance has been minimum. This suggests that sodium vanadate, depending on the compositional phase resistance of the three stabilizers, has shown a different extent of reaction with the three sintered samples.

3.5. *Morphology of sintered sample after hot corrosion test*

Fig. 12 displays a FESEM image from the surface of sintered samples after the corrosion test.

According to the EDS results, the rod-shaped corrosion products are seen resulting from YVO_4 crystals plus pseudocubic crystals with varying sizes resulting from CeO_2 exiting from the zirconia lattice on the surface of the sintered pellet form. According to Fig. 12a, the length of rod-shaped YVO_4 formed in nanoYSZ and $(ScCeYSZ)_2$ was higher than in other samples due to more leaching of Y element from both samples.

EDS analysis (Fig. 12) has been done to confirm the chemical compounds of corrosion products. EDS results obtained from the specified region (Fig. 12d) from the $(ScCeYSZ)_1$ sample show that the rod-shaped crystals formed on the surface of the sintered pellet have mostly been composed of V, Y, and O elements with atomic percentages of 25.92%, 11.55%, and 3.88% respectively. XRD analysis also confirmed the formation of the YVO_4 phase.

EDS results obtained from the specified region in Fig. 13 from $(ScCeYSZ)_{1\text{-}3}$ samples show that the cubic crystals formed on the surface of the sintered pellets mostly consist of Ce elements.

Also, based on the EDS results regarding the substrate of this sample (Fig. 13c), it consists of Zr and O elements. The SEM image of the sintered samples $(ScCeYSZ)_2$ and $(ScCeYSZ)_3$ also shows rod-shaped crystals similar to the $(ScCeYSZ)_1$ sample on the surface of the sample. The corrosion products are mostly present in the nanoYSZ sample with larger dimensions, while the extent of corrosion has diminished in the $(ScCeYSZ)_3$ sample. The FESEM image of the nanoYSZ sample shows the formation of corroded crystals. The results reveal that the length and diameter of the rod-like particles formed in the nanoYSZ sample have been larger than that of $(ScCeYSZ)_{1\text{-}3}$ samples.

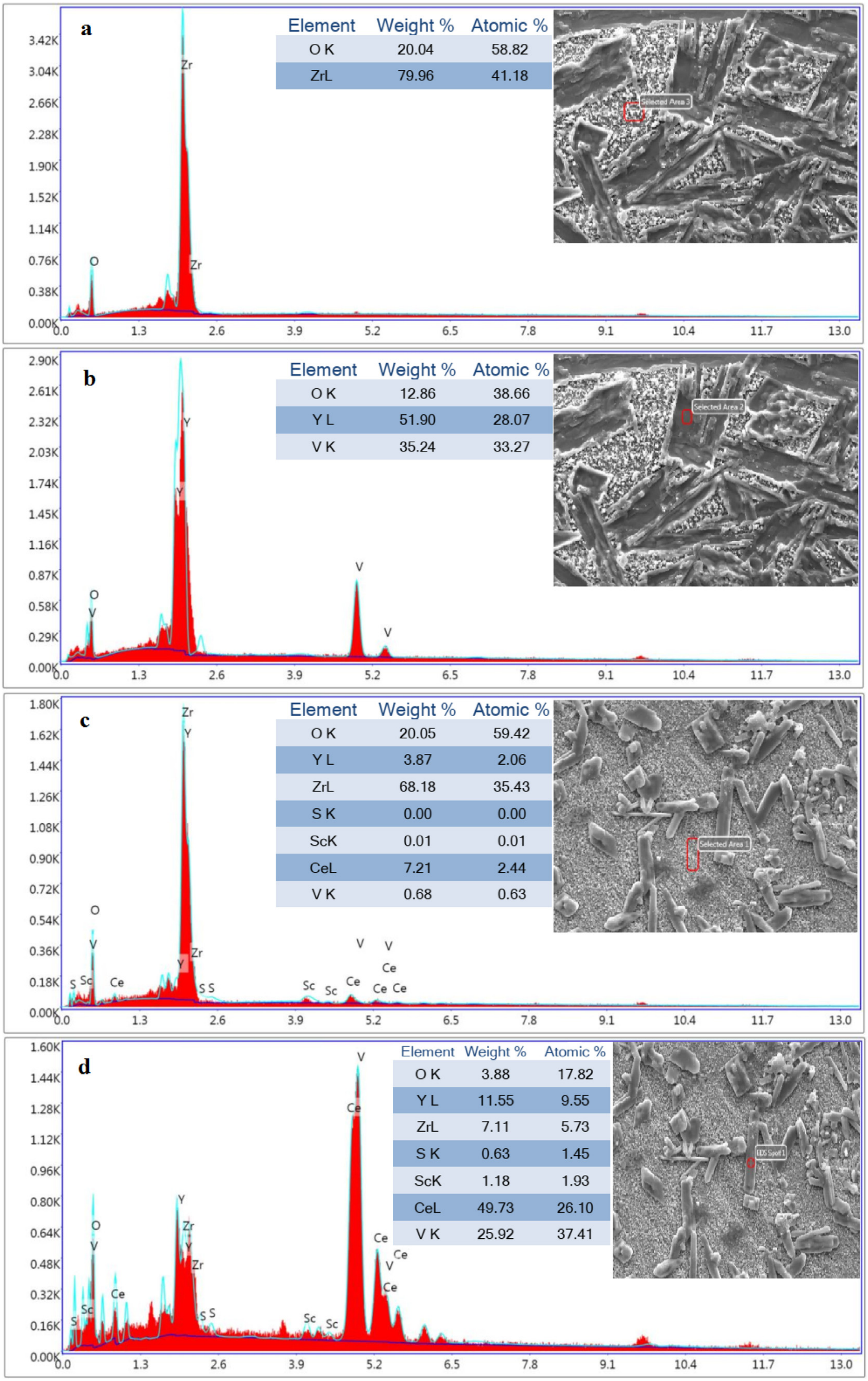

a

Element	Weight %	Atomic %
O K	20.04	58.82
ZrL	79.96	41.18

b

Element	Weight %	Atomic %
O K	12.86	38.66
Y L	51.90	28.07
V K	35.24	33.27

c

Element	Weight %	Atomic %
O K	20.05	59.42
Y L	3.87	2.06
ZrL	68.18	35.43
S K	0.00	0.00
ScK	0.01	0.01
CeL	7.21	2.44
V K	0.68	0.63

d

Element	Weight %	Atomic %
O K	3.88	17.82
Y L	11.55	9.55
ZrL	7.11	5.73
S K	0.63	1.45
ScK	1.18	1.93
CeL	49.73	26.10
V K	25.92	37.41

Fig. 12 Spot-EDS analysis from the matrix and rod-like shape of (a-b) nano8YSZ sample, (c-d) $(ScCeYSZ)_1$ sample, (e-f) $(ScCeYSZ)_2$ sample, and (g-h) $(ScCeYSZ)_3$ disc-shaped sample after hot corrosion test.

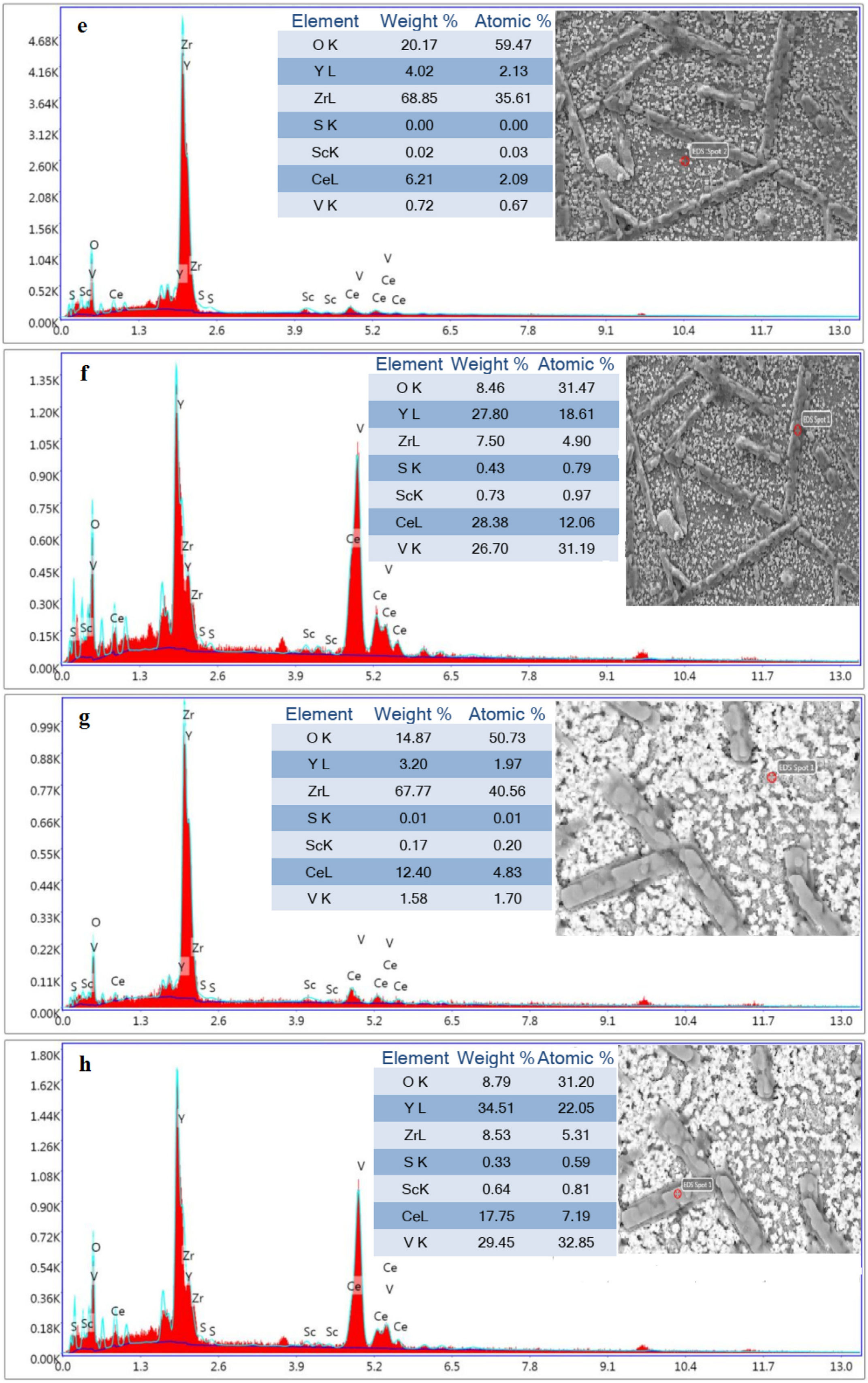

e

Element	Weight %	Atomic %
O K	20.17	59.47
Y L	4.02	2.13
ZrL	68.85	35.61
S K	0.00	0.00
ScK	0.02	0.03
CeL	6.21	2.09
V K	0.72	0.67

f

Element	Weight %	Atomic %
O K	8.46	31.47
Y L	27.80	18.61
ZrL	7.50	4.90
S K	0.43	0.79
ScK	0.73	0.97
CeL	28.38	12.06
V K	26.70	31.19

g

Element	Weight %	Atomic %
O K	14.87	50.73
Y L	3.20	1.97
ZrL	67.77	40.56
S K	0.01	0.01
ScK	0.17	0.20
CeL	12.40	4.83
V K	1.58	1.70

h

Element	Weight %	Atomic %
O K	8.79	31.20
Y L	34.51	22.05
ZrL	8.53	5.31
S K	0.33	0.59
ScK	0.64	0.81
CeL	17.75	7.19
V K	29.45	32.85

Fig. 12 (*continued*)

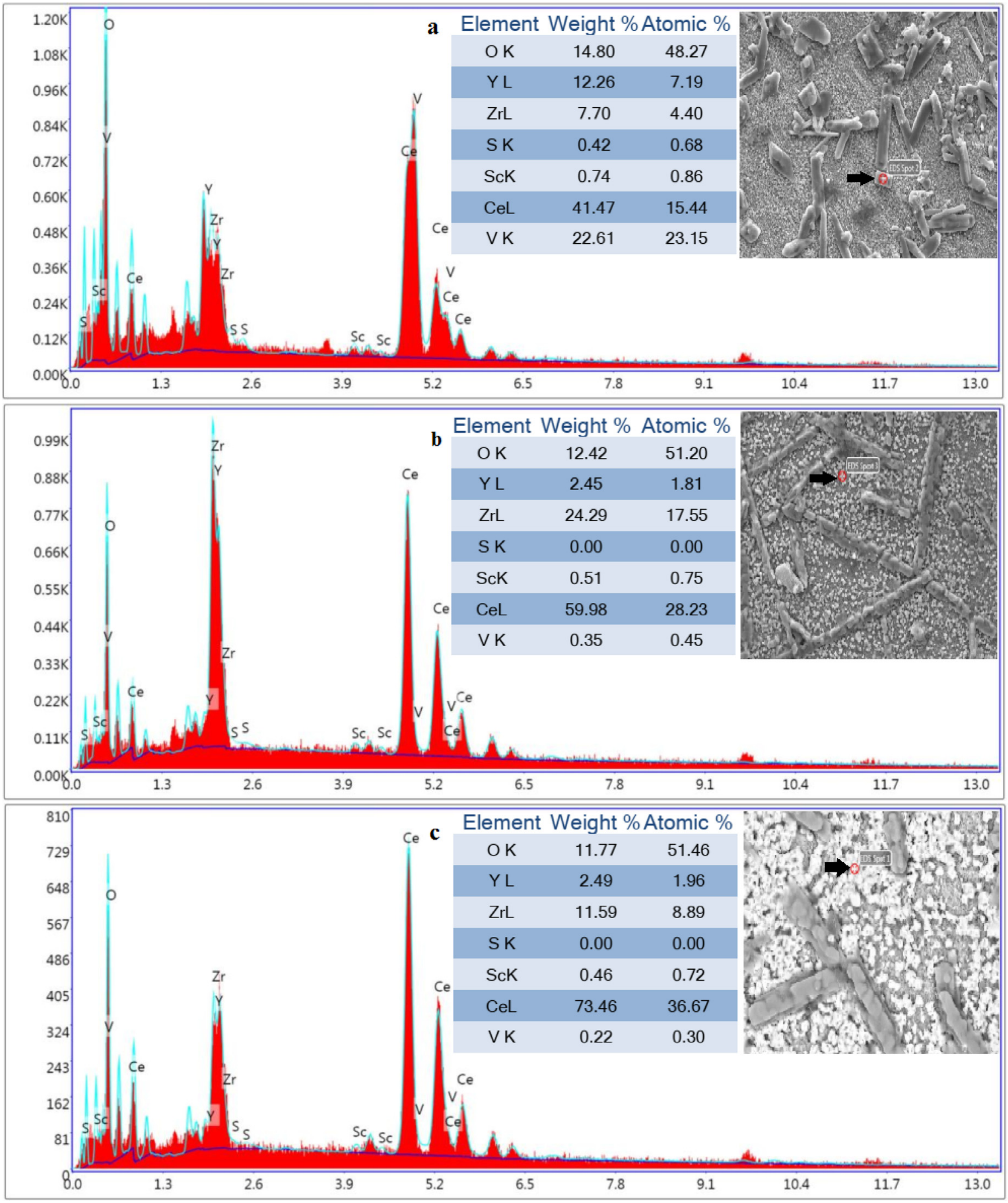

a

Element	Weight %	Atomic %
O K	14.80	48.27
Y L	12.26	7.19
ZrL	7.70	4.40
S K	0.42	0.68
ScK	0.74	0.86
CeL	41.47	15.44
V K	22.61	23.15

b

Element	Weight %	Atomic %
O K	12.42	51.20
Y L	2.45	1.81
ZrL	24.29	17.55
S K	0.00	0.00
ScK	0.51	0.75
CeL	59.98	28.23
V K	0.35	0.45

c

Element	Weight %	Atomic %
O K	11.77	51.46
Y L	2.49	1.96
ZrL	11.59	8.89
S K	0.00	0.00
ScK	0.46	0.72
CeL	73.46	36.67
V K	0.22	0.30

Fig. 13 Spot-EDS analysis from cubic morphology of (a) $(ScCeYSZ)_1$, (b) $(ScCeYSZ)_2$, and $(ScCeYSZ)_3$ disc-shaped samples after hot corrosion test.

Fig. 14 shows the cross-section of the samples after the hot corrosion test. As it is clear in the pictures, all samples $(ScCeYSZ)_{1\text{-}3}$ and nanoYSZ have corroded areas. The corroded and reacted areas with molten salt are more in the nanoYSZ samples than in other samples. Also, the rod-shaped crystals of yttrium vanadate can be seen in the cross-section of the nanoYSZ sample. The reason for it can be the fact the rod-shaped crystals are larger than. $(ScCeYSZ)_{1\text{-}3}$ samples. The formation of holes and cracks is the result of corrosion products. Furthermore, the depth of molten salts for $(ScCeYSZ)_1$ (100–150 µm) was lower than in other samples. According to Fig. 14, the percentage of holes in the nanoYSZ body (45%) was higher than $(ScCeYSZ)_{1\text{-}3}$ sample (($(ScCeYSZ)_1$: 15%, (($(ScCeYSZ)_2$: 34% and $(ScCeYSZ)_3$: 25%).

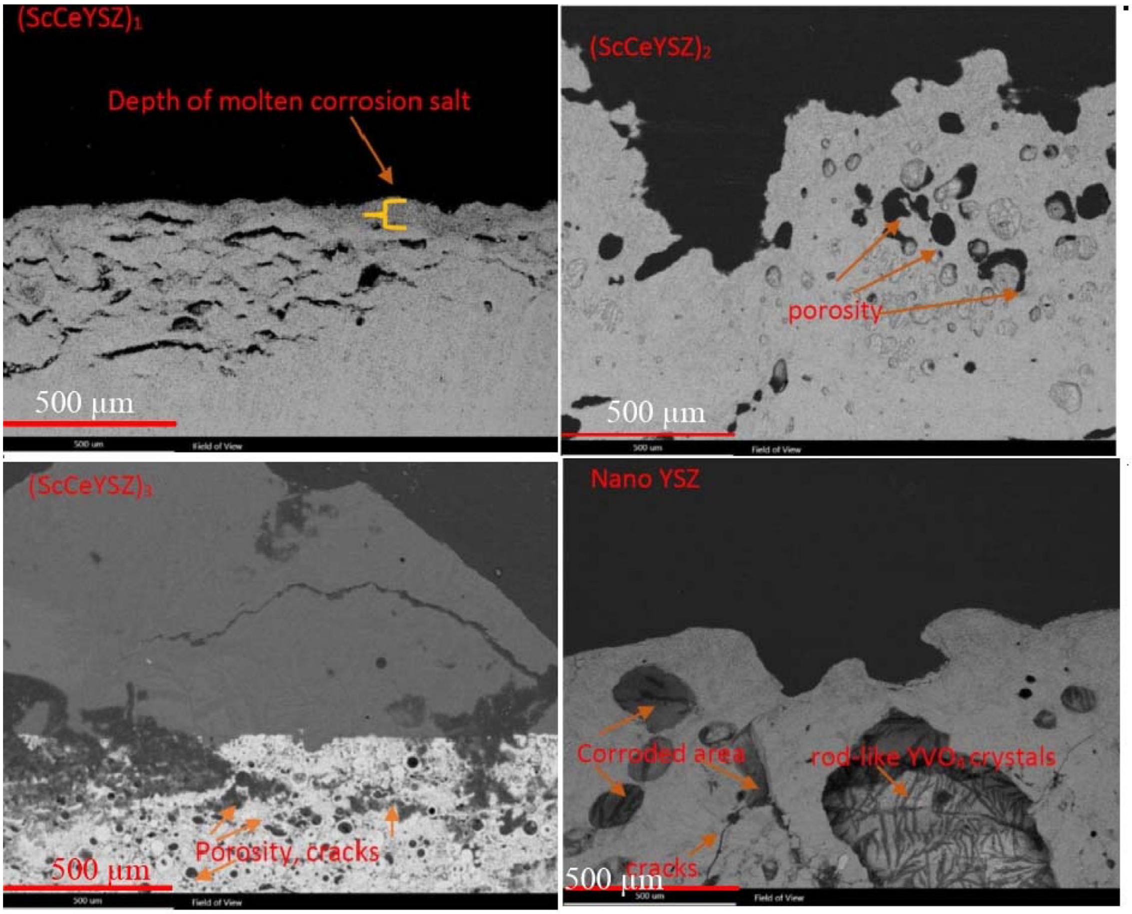

Fig. 14 Cross-sectional FESEM image (Back scattering mode) of sintered samples after the hot corrosion test.

3.6. Mechanism analysis

In the first stage, a mix of sodium sulfate and vanadium oxide molten salts reacted at high temperatures, whereby the intermediate product of $NaVO_3$ (Reaction # 1), which has a low melting point of about 610 °C is formed (Jalil Abduladheem et al., 2021; Li et al., 2021).

$$Na_2SO_{4(l)} + V_2O_{5(l)} \rightarrow 2NaVO_{3(l)} + SO_{3(g)} \quad (1)$$

The reaction between $NaVO_3$ and the stabilizers present in the zirconia is based on the Lewis acid-base law. Among stabilizers (Sc^{+3}, Ce^{+4}, Y^{+3} as a Lewis acid element), V_2O_5 (as a Lewis acid compound) preferably reacts with Y^{+3}, causing leaching of stabilizers from inside the zirconia structure. Thus, it forms the corrosion products of YVO_4 (reaction # 2) and (m-ZrO_2) ZrO_2 monoclinic product (Raya et al., 2022a; Jones, 1997; Park et al., 2005). Sc_2O_3 has more acidic nature properties and causes less reactivity with the Lewis acidic metal oxide, such as the V_2O_5 compound. Experimental research has shown that CeO_2, due to greater acidity over Y_2O_3, is more resistant to reaction with $NaVO_3$. However, reports (Park et al., 2005; Ahmadi-Pidani et al., 2012; Habibi et al., 2012; Zhong et al., 2010; Yasuda et al., 2004; Liu et al., 2023; Fu et al., 2020; Abosaooda et al., 2021; Yuhua et al., 2017; Chen et al., 2020; Qiu et al., 2023; Jones and Williams, 1987; Zhao, 2022; Liu et al., 2022; Park et al., 2005) showed that $NaVO_3$ reacts with the Ce^{+4} present in zirconia to form $CeVO_4$ (reaction # 3).

$$ZrO_2.Y_2O_3 + NaVO_3 \rightarrow m\text{-}ZrO_2 + YVO_4 + Na_2O \quad (2)$$

$$ZrO_2.CeO_2 + NaVO_3 \rightarrow m\text{-}ZrO_2 + CeVO_4 + Na_2O \quad (3)$$

Park et al. conducted research on the corrosion resistance of zirconia with one stabilizer agent (ceria stabilized zirconia (CSZ) and yttria-stabilized zirconia YSZ compounds). Their study showed that the CSZ has a higher corrosion resistance than YSZ (Park et al., 2005).

Jones et al. investigated the corrosion resistance of different stabilizer agents doped in zirconia lattice. In their research, they compared the reactivity of Sc_2O_3, Y_2O_3, CeO_2 and Ta_2O_5 stabilizing elements. Among several introduced oxides, Sc_2O_3 has the least reactivity with corrosive salts (Jones and Williams, 1987).

According to the obtained results, zirconia stabilized with yttria-ceria-scandia (ScCeYSZ) has higher corrosion resistance than other works with one or two stabilizer agents. The percent of YVO_4 and monoclinic phase in the $(ScCeYSZ)_1$ sample was lower than in other works (Song et al., 2023; Jalil Abduladheem et al., 2021; Li et al., 2021; Viazzi et al., 2006).

It was probably due to the higher Lewis acid nature of the mixture of Sc^{3+}:Ce^{4+}:Y^{3+} element (ScCeYSZ) and better tetragonality percent than YSZ ceramics and reports were done about CYSZ, CSZ and ScSZ ceramics (Khaki et al., 2022; Habibi and Guo, 2015; Chen et al., 2019; Bokov et al., 2021; Hajizadeh-Oghaz et al., 2016; Jamali et al., 2014; Park et al., 2005; Ahmadi-Pidani et al., 2012; Habibi et al., 2012).

4. Conclusion

Zirconia samples stabilized with Sc_2O_3, Y_2O_3, and CeO_2 samples were synthesized with various weight percentages through the sol–gel method. FESEM images confirmed the nanoscale nature of the synthesized particles with an average particle size of 80–90 nm. XRD pattern showed that with increasing scandium oxide and reducing ceria content, the percentage of the tetragonal phase of zirconia was increased. Among 13 samples in Table 1, $Sc_{1.8}Ce_{8.3}Y_{1.9}SZ$ nanopowders had the highest phase stability at 1600 °C. The $C/a\sqrt{2}$ the parameter in these samples showed that the $(ScCeYSZ)_1$ sample had the highest t́ phase.

Results of the hot corrosion test show that the sample with a higher amount of acidic oxide (scandia) has more resistance to stabilizer leaching from the zirconia lattice. Despite more porosity (theoretical density of 98.9%) in $(ScCeYSZ)_1$ body than $(ScCeYSZ)_{2,\ 3}$ samples, the amount of ceria and yttria leaching in the form of polygonal and rod-like shapes was lower than other samples.

Furthermore, due to the larger rod size of YVO_4 crystals in the nanoYSZ body and more leaching of yttria from the YSZ sintered body, YSZ ceramics show less hot corrosion resistance than $(ScCeYSZ)_{1,3}$ samples.

CRediT authorship contribution statement

Mina Aflaki: Conceptualization, Data curation, Investigation, Methodology, Project administration. **Fatemeh Davar:** Conceptualization, Data curation, Investigation, Methodology, Project administration. **Mohammad Reza Loghman Estarki:** Conceptualization, Data curation, Investigation, Methodology, Project administration. **Ruixue Wang:** Conceptualization, Methodology, Project administration. **Lei Guo:** Conceptualization, Methodology, Project administration.

Declaration of Competing Interest

The authors declare that they have no known competing financial interests or personal relationships that could have appeared to influence the work reported in this paper.

Acknowledgement

The authors thanked the Isfahan University of Technology for the financial support of the PhD thesis of Dr Mina Aflaki (current work).

Ethics approval

This study was not performed on Animals/Humans.

Consent for publication

All authors have given consent for submitting this paper to Journal.

Availability of data and materials

The data will be available after the request.

Funding

The authors are grateful to the Isfahan University of Technology for providing financial support.

Appendix A. Supplementary material

Supplementary data to this article can be found online at https://doi.org/10.1016/j.arabjc.2023.105160.

References

Abosaooda, M., Majid Wajdy, J., Hussein, E.A., Jalil, A.T., Kadhim, M.M., Abdullah, M.M., Hamed, A.H., Almashhadani, H.A., 2021. Role of vitamin C in the protection of the gum and implants in the human body: theoretical and experimental studies. Int. J. Corros. Scale Inhibit. 10, 1213–1229.

R. Ahmadi-Pidani, R. Shoja-Razavi R, R. Mozafarinia , H. Jamali. Evaluation of hot corrosion behavior of plasma sprayed ceria and yttria-stabilized zirconia thermal barrier coatings in the presence of $Na_2SO_4 + V_2O_5$ molten salt, Ceram. Int. 38 (2012) 6613–6620.

Ahsanzadeh-Vadeqani, M., Razavi, R.S., 2016. Spark plasma sintering of zirconia-doped yttria ceramic and evaluation of the microstructure and optical properties. Ceram. Int. 42, 18931–18936.

Al-Zuhairy, S.A., Kadhum, W.R., Alhijjaj, M., Kadhim, M.M., Al-Janabi, A.S., Salman, A.W. . . . Khadom, A.A., 2022. Development and Evaluation of Biocompatible Topical Petrolatum-liquid Crystal Formulations with Enhanced Skin Permeation Properties. J. Oleo Sci. 71 (3), 459–468.

Bakhshkandi, R., Ghoranneviss, M., 2019. Investigating the synthesis and growth of titanium dioxide nanoparticles on a cobalt catalyst. J. Res. Sci. Eng. Technol. 7, 1–3.

Bat-Ulzii, J., Omoontsoo, G., Lygdenov, B.D., Purevsuren, T., 2023. In situ production of B4C and FeV enriched composite surface on low carbon steel by cast sintering technique. Metall. Mat. Eng. 29, 70–79.

D. Bokov, et al., Nanomaterial by sol-gel method: synthesis and application. Adv. Mat. Sci. Eng. 2021 (2021) 1-21 (b) R. Ahmadi-Pidani, R. Shoja-Razavi, R. Mozafarinia, H. Jamali, Evaluation of hot corrosion behavior of plasma sprayed ceria and yttria-stabilized zirconia thermal barrier coatings in the presence of $Na_2SO_4 + V_2O_5$ molten salt, Cerami. Int. 38 (2012) 6613–6620.

Budi, H.S., Davidyants, A., Rudiansyah, M., Javed Ansari, M., Suksatan, W., Sultan, M.Q., Turki Jalil, A., Kazemnejadi, M., 2022. Alendronate reinforced polycaprolactone-gelatin-graphene oxide: A promising nanofibrous scaffolds with controlled drug release. Mat. Today Commun. 32, 104108.

Y. Chen, S. Sun, T. Zhang, Xi. Zhou, and S. Li. Effects of post-weld heat treatment on the microstructure and mechanical properties of laser-welded NiTi/304SS joint with Ni filler. Mat. Sci. Eng. A 771 (2020) 138545.

Chen, C., Liang, T., Guo, Y., Chen, X., Man, Q., et al, 2019. Effect of Scandia content on the hot corrosion behavior of Sc_2O_3 and Y_2O_3 co-doped ZrO_2 in $Na_2SO_4 + V_2O_5$ molten salts at 1000 °C. Corros. Sci. 158, 108094–108194.

Chen, J., Zhang, Z., Lu, H., 2022. Structure design and properties investigation of Bi2O2Se/graphene van der Waals heterojunction from first-principles study. Surf. Interfac. 33, 102289.

Chen, Z., Zhong, W., Liu, S., Zou, T., Zhang, K., Gong, C., Wang, H., 2023. Highly Stereodivergent Synthesis of Chiral C4-Ester-Quaternary Pyrrolidines: A Strategy for the Total Synthesis of Spirotryprostatin A. Organic Lett 25 (19), 3391–3396.

Chupradit, S., Nasution, M.K., Rahman, H.S., Suksatan, W., Jalil, A. T., Abdelbasset, W.K., Bidares, R., 2022. Various types of electrochemical biosensors for leukemia detection and therapeutic approaches. Ana. Biochemi. 654, 114736.

Davar, F., Loghman-Estarki, M.R., 2014. Synthesis and optical properties of pure monoclinic zirconia nanosheets by a new precursor. Ceram. Int. 40, 8427–8433.

Dayal, R., Gokhale, N.M., Sharma, S.C., Krishnan, R., 1992. Investigation of the metastable tetragonal phase in yttria-doped zirconia powders prepared by a sol–gel technique. British Ceram. Transact. 91, 45–47.

Dmytro, S.T.R.O.I.A.N.O.V.S.K.Y.I., 2020. The study of welding requirements during construction and installation of seismic-resistant steel structures. J. Res. Sci. Engin. Technol. 8 (2), 17–20.

Dong, P., Zhang, Y., Zhu, S., Nie, Z., Ma, H., Liu, Q., Li, J., 2022. First-principles study on the adsorption characteristics of corrosive species on passive film TiO_2 in a NaCl solution containing H_2S and CO_2. Metals 12, 1160.

Fu, Z.H., Yang, B.J., Shan, M.L., Li, T., Zhu, Z.Y., Ma, C.P., Zhang, X., Gou, G.Q., Wang, Z.R., Gao, W., 2020. Hydrogen embrittlement behavior of SUS301L-MT stainless steel laser-arc hybrid welded joint localized zones. Corros. Sci. 164, 108337.

Grabis, J., Jankovica, D., Steins, I., Lubane, M., Sīpola, I., 2018. Characteristics and sinter ability of Ceria stabilized zirconia nanoparticles prepared by chemical methods. Mater. Sci. 24, (3).

Guo, L., Zhang, C.L., He, Q., Li, Z.H., Yu, J.X., Liu, X.C., Ye, F.X., 2019. Corrosion products evolution and hot corrosion mechanisms of $REPO_4$ (RE = Gd, Nd, La) in the presence of V_2O_5 + Na_2SO_4 molten salt. J. Europ. Ceram. Soc. 39, 1496–1506.

Habibi, M.H., Guo, S.M., 2015. The hot corrosion behavior of plasma sprayed zirconia coatings stabilized with yttria, ceria, and titania in sodium sulfate and vanadium oxide. Mater. Corros. 66, 270–277.

Habibi, M.H., Wang, L., Guo, S.M., 2012. Evolution of hot corrosion resistance of YSZ, $Gd_2Zr_2O_7$, and $Gd_2Zr_2O_7$ + YSZ composite thermal barrier coatings in $Na_2SO_4 + V_2O_5$ at 1050 °C. J. Europ. Ceram. Soc. 32, 1635–1642.

Hajizadeh-Oghaz, M., Shoja Razavi, R., Ghasemi, A., Valefi, Z., 2016. Na_2SO_4 and V_2O_5 molten salts corrosion resistance of plasma-sprayed nanostructured ceria and yttria co-stabilized zirconia thermal barrier coatings. Ceram. Int. 42, 5433–5446.

Huang, W.W., Qiu, H.J., Zhang, Y.Q., et al, 2022. Microstructure and phase transformation behavior of Al_2O_3-ZrO_2 under microwave sintering. Ceram. Int. 49 (49), 4855–4862.

Jalil Abduladheem, T., Al Qurabiy, H.E., Hussain Dilfy, S., Meza, S. O., Aravindhan, S., Kadhim, M.M., Aljeboree, A.M., 2021. CuO/ZrO_2 nanocomposites: facile synthesis, characterization and photocatalytic degradation of tetracycline antibiotic. J. Nanostruct. 11, 333–346.

Jamali, H., Mozafarinia, R., Shoja-Razavi, R., Ahmadi-Pidani, R., 2014. Comparison of hot corrosion behaviors of plasma-sprayed nanostructured and conventional YSZ thermal barrier coatings exposure to molten vanadium pentoxide and sodium sulfate. J. Europ. Ceram. Soc. 34, 485–492.

Jasim, S.A., Hachem, K., Abed Hussein, S., Turki Jalil, A., Hameed, N.M., Dehno Khalaji, A., 2022a. New chitosan modified with epichlohydrin and bidentate Schiff base applied to removal of Pb^{2+} and Cd^{2+} ions. J. Chin. Chem. Soc. 69 (7), 1051–1059.

Jasim, S.A., Hadi, J.M., Catalan Opulencia, M.J., Karim, Y.S., Mahdi, A.B., Kadhim, M.M., Bokov, D.O., Turki Jalil, A., Fakri Mustafa, Y., Falih, K.T., 2022b. MXene/metal and polymer nanocomposites: preparation, properties, and applications. J. Alloys Compds. 917, 165404.

Jasim, S.A., Hadi, J.M., Jalil, A.T., Catalan Opulencia, Hammid, A. T., Tohidimoghadam, M., Moghaddam-Manesh, M., 2022c. Electrospun Ta-MOF/PEBA nanohybrids and their CH_4 adsorption application. Front. Chem. 10, 868794.

Jiang, K., Liu, S., Wang, X., 2018. Low–thermal–conductivity and high–toughness CeO_2–Gd_2O_3 co–stabilized zirconia ceramic for potential thermal barrier coating applications. J. Europ. Ceram. Soc. 38, 3986–3993.

Jones, R.L., 1997. Some aspects of the hot corrosion of thermal barrier coatings. J. Thermal Spray Technol. 6 (I), 77–84.

Jones, R.L., Reidy, R.F., Mess, D., 1996. Scandia, Yttria-stabilized zirconia for thermal barrier coatings. Surf. Coat. Technol. 82, 70–76.

Jones, R.L., Williams, C.E., 1987. Hot corrosion of zirkonia ceramics. Surf. Coat. Technol. 32, 349–358.

Kadhim, M.M., Sead, F.F., Jalil, A.T., Taban, T.Z., Rheima, A.M., Almashhadani, H.A., Hamel, S., 2022. Al-, Ga-, and In-decorated BP nanotubes as chemical sensors for 2-chloroethanol. Monatshefte für Chemie-Chemical Monthly 153 (7), 589–596.

Kadhum, W.R., Al-Zuhairy, S.A., Mohamed, M.B., Abdulrahman, A. Y., Kadhim, M.M., Alsadoon, Z., Teoh, T.C., 2021. A Nanotechnological Approach for Enhancing the Topical Drug Delivery by Newly Developed Liquid Crystal Formulations. A Nanotechnological Approach for Enhancing the Topical Drug Delivery by Newly Developed Liquid Crystal FormulationsI. JDDT 11 (3), 716–721.

Kadhum, W.R., See, G.L., Alhijjaj, M., Kadhim, M.M., Arce, F.J., Al-Janabi, A.S., Khadom, A.A., 2022. Evaluation of the Skin Permeation-Enhancing Abilities of Newly Developed Water-Soluble Self-Assembled Liquid Crystal Formulations Based on Hexosomes. Crystals 12 (9), 1238.

Kanade, K.G., Baeg, J.O., Apte, S.K., Prakash, T.L., Kale, B.B., 2008. Synthesis and characterization of nanocrystallined zirconia by hydrothermal method. Mat. Res. Bull. 43, 723–729.

N. Khaki, et al., Sensing of acetaminophen drug using Zn-doped boron nitride nanocones: a DFT inspection. Appl. Biochem. Biotechnol. 194 (2022) 2481-2491. (b) R. Ahmadi-Pidani, R. Shoja-Razavi, R. Mozafarinia, H. Jamali, Comparison of Hot Corrosion Resistance of YSZ and CYSZ Thermal Barrier Coatings in Presence of Sulfate-Vanadate Molten Salts, Advan. Mater. Research. 472-475 (2012) 141-144.

Kartika, R., Alsultany, F.H., Jalil, A.T., Mahmoud, M.Z., Fenjan, M. N., Rajabzadeh, H., 2022. $Ca_{12}O_{12}$ nanocluster as highly sensitive material for the detection of hazardous mustard gas: Density-functional theory. Inorg. Chem. Commun. 137, 109174.

Kikuchi, S., Katahira, K., Komotori, J., 2018. Formation of Titanium/Zirconia based biomaterial fabricated by spark plasma sintering. J. Japan Inst. Met. Mater. 82, 341–348.

Li, G., Huang, S., Li, K., Zhu, N., Zhao, B., Zhong, Q., Zhang, Z., Ge, D., Wang, D., 2022. Near-infrared responsive Z-scheme heterojunction with strong stability and ultra-high quantum efficiency constructed by lanthanide-doped glass. Appl. Catal. B: Env. 311, 121363.

Li, S., Xu, S.h., Wang, X., Wang, D., Goodman, B.A., et al, 2021. Optical properties of gadolinia-doped cubic yttria-stabilized zirconia single crystals. Ceram. Int. 47, 3346–3353.

H. f. Liu, X. Xiong, X. b. Li, Y. l. Wang, Hot corrosion behavior of Sc_2O_3–Y_2O_3–ZrO_2 thermal barrier coatings in presence of Na_2SO_4 + V_2O_5 molten salt, Mater. Corros. 85 (2014) 87–93.

B. Liu, I. Khalid, I. Patra, O. R. Kuzichkin, R.Sivaraman, A. T., Jalil, M. Hekmatifar, The effect of hydrophilic and hydrophobic surfaces on the thermal and atomic behavior of ammonia/copper nanofluid using molecular dynamics simulation. J.Mol. Liquids, 364 (2022) 119925.

Liu, Y., Fan, B., Bin, X.u., Yang, B., 2023. Ambient-stable polyethyleneimine functionalized Ti3C2Tx nanohybrid corrosion inhibitor for copper in alkaline electrolyte. Mater. Lett. 337, 133979.

Lughiw, V., Clarke, D.R., 2005. Transformation of electron-beam physical vapor-deposited 8 wt% Yttria-stabilized Zirconia thermal barrier coatings. J. Am. Ceram. Soc. 88, 2552–2558.

K. Nakamoto, Infrared and Raman Spectra of Inorganic and Coordination compounds, Handbook of Vibrational Spectroscopy, John Wiley & Sons, Ltd, New York. (2006) 1872–1892.

Obaid, R.F., Kadhim Hindi, Kadhum, S.A., Jafaar Alwaeli, Jalil, A. T., 2022. Antibacterial activity, anti-adherence and anti-biofilm activities of plants extracts against Aggregatibacter actinomycetemcomitans: An in vitro study in Hilla City, Iraq. Caspian J. Env. Sci. 20 (2), 367–372.

Park, S.Y., Kim, J.H., Kim, M.C., Song, H.S., Park, C.G., 2005. Microscopic observation of degradation behavior in yttria and ceria stabilized zirconia thermal barrier coatings under hot corrosion. Surf. Coat. Technol. 190, 357–365.

Qiu, R., Wang, W., Wang, Z., Wang, H., 2023. Advancement of modification engineering in lean methane combustion catalysts based on defect chemistry. Catal. Sci. Technol. 13, 2566–2584.

Radjehi, L., Aissani, L., Djelloul, A., Saoudi, A., Lamri, S., Nomenyo, K., Lerondel, G., Sanchette, F., 2023. Air and vacuum annealing effect on the highly conducting and transparent properties of the undoped zinc oxide thin films prepared by DC magnetron sputtering. Metall. Mat. Eng. 29, 37–51.

Rashad, M.M., Baioumy, H.M., 2008. Effect of thermal treatment on the crystal structure and morphology of zirconia nanopowders produced by three different routes. J. Mat. Proc. Technol. 195, 178–185.

Raya, I., Chupradit, S., Kadhim, M.M., Mahmoud, M.Z., Turki Jalil, A., Surendar, A., Tuama Ghafel, S., Fakri Mustafa, Y., Bochvar, A.N., 2022a. Role of compositional changes on thermal, magnetic, and mechanical properties of Fe-PC-based amorphous alloys. Chin. Phys. B 31, 016401.

Raya, I., Chupradit, S., Mustafa, Y.F., H Oudaha, K., M Kadhim, M., Turki Jalil, A., Thangavelu, L., 2022b. Carboxymethyl Chitosan Nano-Fibers for Controlled Releasing 5-Fluorouracil Anticancer Drug. J. Nanostruct. 12 (1), 136–143.

Ritasalo, R., Cura, M.E., Liu, X.W., Ge, Y., Kosonen, T., Kanerva, U., Soderberg, O., Hannula, S.P., 2013. Microstructural and mechanical characteristics of Cu–Cu_2O composites compacted with pulsed electric current sintering and hot isostatic pressing. Compos. Part A: Appl. Sci. Manuf. 45, 61–69.

Rocha, J., Alvarado-Orazo, J.M., Gomez, P.A., et al, 2022. Hot corrosion behavior of dense CYSZ/YSZ bilayer coatings deposited by atmospheric plasma spray in $Na_2SO_4 + V_2O_5$ molten salts. Surf. Coat. Technol. 432, 128066.

M. Sadeghi, et al., Dichlorosilane adsorption on the Al, Ga, and Zn-doped fullerenes Monatshefte für Chemie-Chemical Monthly 153, (2022) 427-434. (b) H.F. Liu, X. Xiong, X.B. Li, Y.L. Wang, Hot corrosion behavior of Sc_2O_3-Y_2O_3-ZrO_2 thermal barrier coatings in the presence of Na_2SO_4 + V_2O_5 molten salt, Corros. Sci. 85 (2014) 87-93.

Salahdin, O.D., Sayadi, H., Solanki, R., Mireya, R., Parra, R., Al-Thamir, M., Turki Jalil, A., Emad Izzat, S., Thaeer Hammid, A., Barboza Arenas, L.A., Kianfar, E., 2022. Graphene and carbon structures and nanomaterials for energy storage. Appl. Phys. A 128, 703.

Seyyedi, M., Molajou, A., 2021. Nanohydroxyapatite loaded-acrylated polyurethane nanofibrous scaffolds for controlled release of paclitaxel anticancer drug. J. Res. Sci. Engin. Technol. 9 (01), 50–61.

Sivaraman, R., Patra, I., Opulencia, M.J.C., Sagban, R., Sharma, H., Jalil, A.T., Ebadi, A.G., 2022. Evaluating the potential of graphene-like boron nitride as a promising cathode for Mg-ion batteries. J. Electroanalyt. Chem. 917, 116413.

Song, Z., Shao, X., Wu, W., Liu, Z., Yang, M., Liu, M., Wang, H., 2023. Structures and stabilities of carbon chain clusters influenced by atomic antimony. Molecules 28, 1358.

Srinivasan, R., De Angelis, R.J., Ice, G., Davis, B.H., 1991. Identification of tetragonal and cubic structures of zirconia using synchrotron x-radiation source. J. Mat. Res. 6, 1287–1291.

Viazzi, C., Bonino, J.P., Ansart, F., Barnabé, A., 2006. Structural study of metastable tetragonal YSZ powder produced via sol–gel route. J. Alloys Compd. 24, 1776–1783.

Yasuda, K., Goto, Y., Takeda, H., 2004. Influence of tetragonality on tetragonal-to monoclinic phase transformation during hydrothermal aging in plasma-sprayed Yttria stabilized Zirconia coatings. J. Am. Ceram. Soc. 84, 1037–1042.

Yuan, J.Y., Zhang, H., Zhou, X., Sun, J.B., Wang, J.S., et al, 2018. Cao, Phase and microstructure evolution of $SrCeO_3$ ceramic when exposed to molten V_2O_5 at 700–1250 °C. Corros. Sci. 145, 295–306.

Yuhua, C., Yuqing, M., Weiwei, L., Peng, H., 2017. Investigation of welding crack in micro laser welded NiTiNb shape memory alloy and Ti6Al4V alloy dissimilar metals joints. Opt. Laser Technol. 91, 197–202.

Yumashev, A.V., Rudiansyah, M., Chupradit, S., Kadhim, M.M., Jalil, A.T., Abdelbasset, W.K., Bidares, R., 2022. Optical-based biosensor for detection of oncomarker CA 125, recent progress and current status. Anal. Biochem. 655, 114750.

Zhang, Z., Hou, Z.W., Chen, H., Li, P., Wang, L., 2023. Electrochemical electrophilic bromination/spirocyclization of N-benzyl-acrylamides to brominated 2-azaspiro [4.5] decanes. Green Chem 25 (9), 3543–3548.

Zhang, B.P., Song, W.J., Wei, L.L., Xiu, Y.X., Xu, H.B., Dingwell, D. B., Guo, H.B., 2019. Novel thermal barrier coatings repel and resist molten silicate deposits. Scripta Mater. 163, 71–76.

Zhao, Y., 2022. Stability of phase boundary between L12-Ni_3Al phases: A phase field study. Intermetallics 144, 107528.

Zhao, C., Fai Cheung, C., Xu, P., 2020. High-efficiency sub-microscale uncertainty measurement method using pattern recognition. ISA Transactions 101, 503–514.

Zhao, G., Hooman, M., Yarigarravesh, M., Algarni, M., Catalan Opulencia, M.J., Alsaikhan, F., Turki Jalil, A., et al, 2022. Vibration analysis of size dependent micro FML cylindrical shell reinforced by CNTs based on modified couple stress theory. Arab. J. Chem. 15, 104115.

Zhao, W., Suo, H.L., Wang, S., Ma, L., Wang, L., Wang, Q., Zhang, Z., 2022. Mg gas infiltration for the fabrication of MgB_2 pellets using nanosized and microsized B powders. J. Europ. Ceram. Soc. 42, 7036–7048.

Zhong, X.H., Wang, Y.M., Xu, Z.H., Zhang, Y.F., et al, 2010. Cao, Hot-corrosion behaviors of overlay-clad yttria-stabilized zirconia coatings in contact with vanadate–sulfate salts. J. Europ. Ceram. Soc. 30, 1401–1408.